Combinatorial and High Throughput Screening of Electrocatalysts for the Oxygen Reduction Reaction in Alkaline Fuel Cells

Guanyu Chen

Submitted in Partial Fulfillment of the Requirements
for the Degree of

Master of Science

Approved by:
Dr. Robert Bruce van Dover
Dr. Héctor D. Abruña

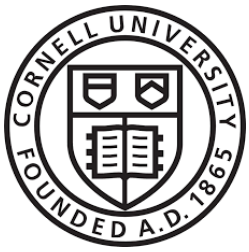

Department of Materials Science and Engineering
Cornell University
Ithaca, New York

[August 2019]
Submitted July 2019

TABLE OF CONTENTS

LIST OF FIGURES

BIOGRAPHICAL SKETCH

Guanyu (also known as Gary) Chen finished his bachelor's degree in Materials Science & Engineering and Philosophy from Rensselaer Polytechnic Institute in 2017. After that, he joined Dr. Bruce van Dover's group in Materials Science and Engineering department at Cornell University focusing on thin film science. This study about fuel cell catalyst is a cooperation project with PhD candidate Yao Yang in Dr. Héctor D Abruña's group. One paper related to this project: *Octahedral spinel electrocatalysts for alkaline fuel cells* has been supplied to PNAS in March 2019; another paper from this project: *Combinatorial and High Throughput Screening of Electrocatalysts for the Oxygen Reduction Reaction in Alkaline Fuel Cells* will be submitted to JACS in August 2019.

ACKNOWLEDGEMENT

First and foremost, I want to thank my advisor Prof. Robert Bruce van Dover for opening the door of thin film science to me. I really appreciate his patience and toleration to my stupid question and irregular working styles. He is like a library, which being knowledgable, kind and always helpful. I also want to thank Prof. Hector D. Abruña for providing supportive advice and serving in my committee.

I want to thank Yao Yang for being a vital partner during the journey. Thanks for showing me the real life of scientific research and teaching me so much in both knowledge and methodology. Also, I want to thank people in van Dover group (Lewis Haber, Duncan Sutherland, Dr. Marc Murphy et al.), Abruña group (Rui Zeng, Yin Xiong et al), Thompson Group and my other peers here (Kaiyang Wang, Ren Zhong etc.) for being good friends with me and share me your wisdom. I will remember the time we have here at Ithaca.

CCMR and CNF are also important parts in my research. My work can not be done without their generous help and training. I want to thank Malcom Thomas and former CCMR employee Dr. Matthew Debney in particular. Thank you for your patience and help.

Next, I want to thank my family who being supportive both financially and mentally to my study in the U.S. There is an old saying in Chinese: “Don’t travel far away and leave your parents waiting and unattending” (父母在不远游). This is my 9th year away from home and yet I still don’t have a plan to go home before I secure a job. Hopefully I won’t let my parents wait for too long.

I like to save the last for my most sincere appreciation, Dr. Jihui Nie. I might save the whole universe in my past life and god allows me to meet you in this life. Thank you for being understanding and supportive about my study, my life, and my decisions. I love you three thousand.

ABSTRACT

This study is an investigation of combinatorial and high throughput screen method for ORR catalyst for alkaline fuel cell. Since the kinetic of alkaline fuel cell ORR is still sluggish, the calling for better catalysts is getting louder. However, the previous screen methods to locating optimal catalytic activity is low efficient. The screen methodology is a combination study of thin film fabrication and electrochemistry where magnetron plasma sputtering has been applied for sample preparation and rotating disk electrode plays an important role in the characterization methodology. The system screened is the palladium (Pd)-3d transitional metal system because Pd shows promising ORR catalytic activity in alkaline media which is comparable with Pt. Previous studies about Pd combined with other 3-d metals exhibit even better activity then single Pd and Pt. Throughout the screen process among the alloys (Pd-Cu, Pd-Co, Pd-Ni, Pd-Fe), we found the $Pd_{50}Cu_{50}$ has the best catalytic activity.

1. INTRODUCTION

This thesis is primarily a study of Oxygen Reduction Reaction (ORR) catalysts in Alkaline Fuel Cell (AFC). The is about utilizing high throughput magnetron plasma sputtering deposition to fabricate thin film catalysts and then study the structural and electrochemical properties of the materials. Palladium-lower-cost 3d-transition-metal alloys (Fe, Co, Ni, Cu, etc.) are being screened to find the composition with optimal catalytic performance.

1.1 Motivation

21st century is a century for technology revolution; human beings have achieved vital breakthroughs in telecommunication, internet, and semiconductors. However, as the main vehicle serves human beings for over a century, internal combustion engine vehicle (ICEV) seems quite stubborn during this tide of revolution. Although many improvements have been made to the ICE to boost the energy conversion efficiency, the engine remains low energy efficiency around 20%; only few specific models can pass 40%. [1] Besides, the emission from ICE is also a problem. About 24% of the world CO_2 emission is from transportation, 75% of which is contributed by road sector (data from 2015).[2] According to the New York State Energy Profile, the average amount of annual emission per vehicle is 4.6 metric ton of CO_2 equivalent ($MtCO_2e$).[3] Considering the social cost of carbon (the quantitative estimation of economic damage caused by carbon emission) [4] is 40$ per pound which is still increasing annually, the average annual social cost of carbon per car is as high as $368,000. That means for every car in the USA, the society needs to pay $368,000 to compensate the damage caused by its carbon emissions. Therefore, actions are deemed to be made to mitigate this loss.

With the phenomenal rise of Tesla Inc., electric vehicle (EV) industry has been experiencing a boom. Compare to ICEVs, EVs have almost zero net emissions and much higher energy efficiency with batteries and electric motors. Also, with less complex mechanics, battery electric vehicle (BEV) and plug-in hybrid electric vehicle (PHEV) require far less maintenance then ICEVs. But EVs are not flawless as well. Customers hold two major concerns about EVs, range anxiety and high capital cost. Many efforts have been applied to solve those two problems, including economics incentives and improvement on Li-ion batteries. However, the compensation incentives can only even the high capital cost and install more charging stations. The relative low battery capacity is the tradeoff of high-power density of the Li-ion batteries. Even though some Tesla models are claimed to have over 300-mile range[5], most of the BEVs on the market today have only 100~200-mile range, which is okay for driving to work inside a city but not good for long distance traveling.[6]

Fuel cell, however, provides another solution for clean energy transportation. Hydrogen fuel cell have gained many attentions as a renewable energy technology to power EVs due to their high energy density, high energy-conversion efficiency and low carbon emission.[7] Compared to traditional ICEs, fuel cell has much higher efficiency (>65%). [8,9] Compared to BEVs, fuel cell electric vehicles (FCEV) have much longer range which is comparable with gasoline cars.[5] The cost of fuel cell has been a hurdle due to the application of noble metal catalyst. For hydrogen fuel cells, the reaction in anode is Hydrogen Oxidation Reaction (HOR) while the reaction in the cathode is Oxygen Reduction Reaction (ORR). The HOR requires only few amount of Platinum (Pt) catalyst while Pt does not work well on the ORR side.[10] A significant amount of Pt (>0.2 g_{Pt}/kW) is still required to catalyze the sluggish oxygen reduction reaction (ORR) so as to provide a power density of >1 W/cm^2 at ≥0.65 V. [11,12,13,14] Since the most effective HOR/ORR catalyst is

still pure Pt, the price of the fuel cell is vibrating with the price of the Pt, which is quite stable and high. Also, because the acid environment in proton-exchange membrane fuel cell (PEMFC), Pt become the only solution for fuel cell catalyst for quite a long time. Due to the alkaline environment within the alkaline fuel cell (AFC), non-precious metal can be used as a replacement for Pt as catalyst. But the KOH electrolyte is easily carbonated and degraded with the presence of carbon. The large-scale commercialization of cheap fuel cell is not possible until the maturity of alkaline electrolyte membrane in AFC. The alkaline membrane replaces KOH liquid electrolyte and dramatically increase the tolerance of carbonation.[9] With this premise, the search for Pt-free ORR catalyst for alkaline fuel cell becomes the one of the motivation of this study.

Among the alternatives for Pt, Palladium (Pd) has gained increasing attention since Pd shows comparable activity to Pt in alkaline media, despite its much lower activity in acidic media. [15] In order to further enhance the ORR activity, tremendous efforts have been devoted to Pd-M alloys to tune the lattice parameters and electronic structures of Pd.[16,17,18,19,20,21] In spite of numerous studies of Pd-based electrocatalysts, the electrocatalytic mechanism has remained poorly understood. To have a comprehensive understanding of Pd-M alloys as an ORR catalyst under alkaline media also becomes a motivation of this study.

The methodology novelty of this research is the adoption of high throughput sputtering methods and rotating disk electrode (RDE). With magnetron sputtering deposition, thin film samples can be fabricated within a relatively short period of time compared to nanoparticle synthesis. At the same time, the nanoparticle samples' ORR activities depend on the synthetic methods employed, particle size, morphology, as well as surface and crystal structures. Those factors are formidable to control simultaneously and complicate the understanding of the intrinsic activities of these electrocatalysts. Consequently, a systematic high throughput combinatorial

approach, with well-controlled morphology and structure, is necessary to assess and evaluate the promising candidate(s) over a variety of Pd-based catalysts. With plasma sputtering, morphology, structure and even composition are well controlled. Two off-axis sputtering guns in opposite directions allows composition gradient spread from 0~100% for both metals of the alloy. RDE provides a direct and rapid method to characterize the catalytic activity. At the same time, this study provides a guideline for a parallel nanoparticle synthesis research. With satisfying materials from sputtered thin film, the parallel nanoparticle synthesis research will be carried on accordingly.

1.2 Fuel Cell

A fuel cell is an electrochemical cell that can convert the chemical energy from the fuel (e.g. hydrogen, hydrazine and natural gas) into electrical energy.[9] Because of the high efficiency and the low emission of fuel cells, tremendous efforts have been devoted to this area to find the key of future “clean energy”. [22]

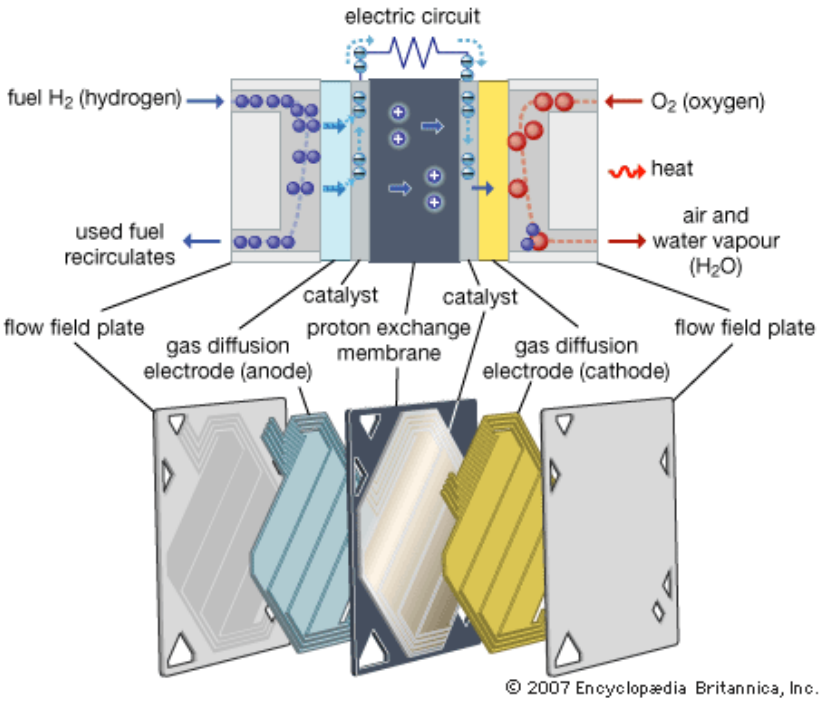

Figure 1.1 ***A structure schematic and reaction process flow of PEMFC. The core parts consist of anode, cathode and the electrolyte membrane in between. Hydrogen is oxide on anode while oxygen is reduced on cathode, during which pure water and heat will be generated as byproducts*** [23]

As a galvanic cell, the structure of the fuel cell is similar with batteries. It is in a form of membrane electrode assembly (MEA) consists of flow field plates, electrolyte membrane and the electrodes. A typical a polymeric electrolyte membrane fuel cell (PEMFC) structure is shown on Figure 1.1.

For the electrochemical reactions in PEMFC, hydrogen will be oxidized on the anode to generate electrons and hydrogen protons which migrate through the ion conductive polymeric electrolyte membrane. Oxygen is reduced on the MEA cathode.

Both HOR and ORR reactions happen on the surface of the catalysts. The byproduct of the overall reaction process is pure water and heat. The gas diffusion electrodes can transport reactants and products water between the flow field plate, which can harvest electros, and the catalyst surface and exchange electrons between them. [7]

However, for alkaline fuel cell the situation is slightly different due to the alkaline electrolyte media which conducts OH^- ions instead of H^+ protons. Thus, the OH^- ions travels to anode and combine with H^+ and generate water and heat on the anode side. [24]

Assuming all the reactions are $4e^-$ reactions, the equation for this Redox reaction is:

Table 1.1 Redox Reaction of PEMFC and AFC (assuming 4e- reactions)

	Anode	Cathode
PEMFC	$H_2 \rightarrow 2H^+ + 2e^-$	$O_2 + 4H^+ + 4e^- \rightarrow 2H_2O$
AFC	$H_2 + 2OH^- - 2e^- \rightarrow 2H_2O$	$O_2 + 2H_2O + 4e^- \rightarrow 4OH^-$

In fact, the ORR reaction can be either $4e^-$ reaction or $2e^-$ reaction depends on the electrocatalytic activity of the catalyst. Strong ORR catalyst can reduce oxygen to O^{2-} which leads to the $4e^-$ reactions to create OH^- or pure water. Otherwise, a $2e^-$ reaction with a mediate step will be introduced where O_2 is reduced to H_2O_2 and then H_2O_2 will be further reduced to form H_2O or OH^-.

1.2.1 Characteristic of Fuel Cell

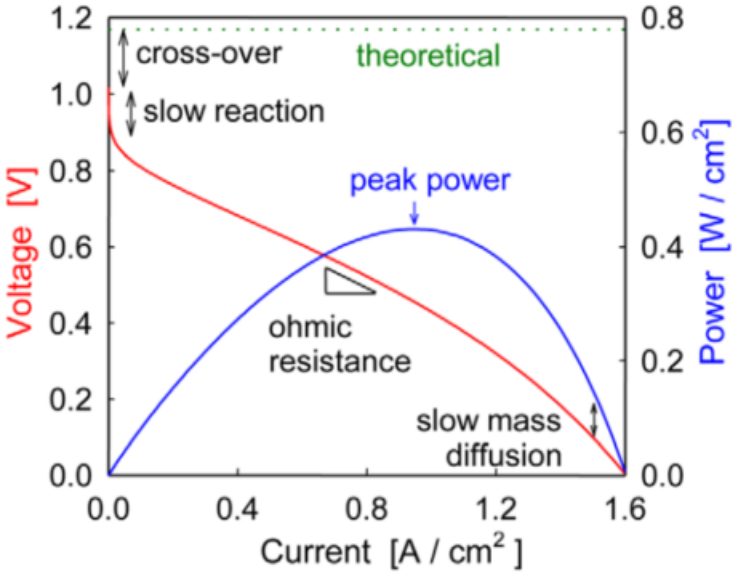

Figure 1.2 *Fuel Cell polarization (red) and power density (blue) curve* [22]

As Figure 1.2 shown, the key characterization parameter is the voltage (V) output as a function of current density (A/cm^2).

$$E = E_{eq} - E_L - \eta_{act} - \eta_{iR} - \eta_{diff} \tag{1.1}$$

The theoretical green dash line is the equilibrium redox potential, or Nernstian voltage at standard condition, E_{eq}.

$$E_{eq} = E_{eq}^{0} - \frac{RT}{nF} ln \ln(Q) \tag{1.2}$$

E_{eq}^{0} is the standard cell potential, and Q is the reaction quotient of the reaction. In reality, the voltage has overpotential drop and decays with increasing current density like the red line. The drop on voltage in different regions of the polarization curve is controlled by different factors.

The cross-over overpotential E_L is due to the gas leak across the electrolyte. The leak could from poor sealing or crack in the electrolyte. Activation overpotential η_{act} dominate high

operation voltage (>0.8V) region. Thus, sluggish reaction in both electrodes will give rise to the η_{act}:

$$\eta_{act} \cong \frac{RT}{\alpha nF} ln \ln\left(\frac{I_0}{I}\right) \tag{1.3}$$

α is the transfer coefficient, the fraction of the overpotential assisting the reaction. I_0 is the current flowing at equilibrium.

η_{iR} is the iR overpotential due to material and interface resistance in the mid-range region. η_{diff} is the overpotential due to mass transportation of the reactants controls the power output in the high electric power density region.

One definition of fuel cell efficiency is the voltage efficiency:

$$\eta = \frac{E}{E_{eq}} \tag{1.4}$$

The challenge in fuel cell catalysts research is to mitigate those loss to sustain high electric power density and high efficiency while lowering the cost of materials. [9]

1.2.2 Alkaline Fuel Cell

As mentioned previously, compare to other types of fuel cells, the main disadvantage of the alkaline fuel cell is the liquid electrolyte is sensitive to the presence of CO_2:

$$CO_2 + 2OH^- \rightarrow CO_3^- + H_2O \tag{1.5}$$

This irreversible carbonation process will poison the electrolyte and disable the fuel cell with increasing number of carbonate formation. Because this reaction modifies the chemical composition of the electrolyte and contracts the number of hydroxyl ions which will migrate to and react at the anode. Consequently, less hydroxyl ions will be transferred to anode and reacted due to both the decrease in ion conductivity of the electrolyte and the quantity of ions. Those lead

to the deterioration of the cell performance. Furthermore, even though this process has no direct degradation impact on the electrodes [25,26], this carbonation reaction will form the precipitation of large metal carbonate crystals (e.g. K_2CO_3) to block the pores of the gas diffusion layer within the electrodes. [27,28]

Therefore, the application of the AFC has been limited to the situation where pure oxygen could be provided until the breakthrough of the anion conducting solid polymeric membrane which replaces liquid KOH solution. [29,30,31] The solid electrolyte membrane has much higher tolerance of CO_2 invasion. In spite of some carbonation happening, no precipitation will migrate with liquid and block the pores of the gas diffusion layer within electrode membranes. Additional advantages about the solid membrane include solvent free conditions, leakproof, and even smaller size and lighter weight. [28]

Because of the breakthrough in the electrolyte and some intrinsic advantages of AFC including relatively low operating temperature (23-70 ^oC) and relative high efficiency (>60%), a great amount of efforts has been devoted to the AFC related topics in the past thirty years. [28] Among those researches, catalyst research in AFC has been one of the hottest topics because the alkaline environment and the rapid kinetics of the electrode reaction enables the application of non-noble metals.[9] There is no doubt that AFC will be a direction for cheap fuel cell option. It is a hope to commercialize fuel cell and bring the world a new kind of abundant, clean energy.

1.2.2.1 ALKALINE ORR CATALYST

ORR in alkaline media is the most complicated electrochemical reaction due to the multiple steps and many different species involved in this four-electron reaction. The reacting mechanism is hard to explain and the rate determination step (RDS) is hard to define. [32] What's more, the kinetics is also influenced by many factors including pH, solvation and polarity of water.[33] As

mentioned previously, two pathways available for the ORR. A direct four-electron reduction pathway for oxygen has a standard reduction potential of 0.41V vs Standard Hydrogen Electrode (SHE) [33]:

$$O_2 + 2H_2O + 4e^- \rightleftharpoons 4OH^-, \quad E^0 = 0.41V\ vs\ SHE \tag{1.6}$$

The two-electron pathway is

$$O_2 + H_2O + 2e^- \rightleftharpoons HO_2^- + OH^-, \quad E^0 = -0.076V\ vs\ SHE \tag{1.7}$$

$$HO_2^- + H_2O + 2e^- \rightleftharpoons 3OH^-, \quad E^0 = 0.878V\ vs\ SHE \tag{1.8}$$

For precious metals, the first step of the reaction is usually being considered as the RDS of the ORR [34,35]:

$$O_2(ad) + e^- \rightarrow O_2^-(ad), \quad E^0 = -0.33V\ vs\ SHE \tag{1.9}$$

This step adsorbs the oxygen species on the surface of the catalyst and break the O-O bond. This interaction is surface sensitive. Therefore, the surface structure of the catalyst and the capability to adsorb oxygen become the key fact for the catalytic performance. [33]

The interaction of oxygen and transition metal can also be explained by d-band theory.[33] The binding energy of the adsorbate with the surface of the transition metal is closely related to the electronic structure, or, d-band of the material. Lima et al. [15] conclude that with higher lying d-band center, the materials will have a stronger bind with oxygen, while lower d-band center materials bind weakly with oxygen. However, strong binding does not necessarily mean better catalytic activity. Pt, which shows the best catalytic activity, exhibits neither too strong nor too weak oxygen adsorption. Therefore, for best activity, the catalyst should have an optimal balance of the d-band center energy. The reaction should also have balance between the kinetics of O-O bond breaking and O-H formation. [15,36]

Since a significant amount of Pt (>0.2 g_{Pt}/kW) is still required to catalyze the sluggish oxygen reduction reaction (ORR) in the AFC, it becomes our interest to develop a Pt free ORR catalyst for AFC. Conventionally, the approaches to increase the catalytic activity and reduce cost include modifying the surface structures and extending the surface area [37,38,39,40,41], alloying [42,43,44], and using supportive materials.[45,46,47] Among those methods, alloying is the most feasible approach with high throughput sputtering. In the case of Pt, additive metals (Co, Ru, Pd etc.) can boost the ORR catalytic activity in alkaline media yet the activity is correlated with the composition of the material.[10,48]

Pd-M bimetallic alloy, gain interest due to the superb activity it shows within the alkaline media; Pd/C has comparable activity with Pt/C while Pd-Pt has even better activity then Pt/C. [15] Previous works about Pd alloys (Pd-Cu, Pd-Co etc.) show that with suitable composition and materials, some Pd-M alloy exhibits activity much better then Pt/C's as an ORR catalyst in alkaline media.[49,50,51,52] However, most of the previous researches are done with nanoparticle synthesis by which composition, crystal structure and surface structure are hard to control. Also, the ORR mechanism stays unknow for those alloys. Therefore, our goal is to screen through the Pd-transition metal bimetallic alloy with high throughput method to find the optimal material for AFC ORR catalyst, and try to have a comprehensive understand of the alloys.

1.3 Magnetron Plasma Sputtering

Magnetron plasma sputtering, as a physical vapor deposition method, utilizing plasma to sputter the atoms off the surface of the solid metal target with energetic ions. The emitted atoms travel across the low-pressure environment and deposit on the substrate to form thin film.[53] Plasma sputtering has always been an efficient way to prepare solid-state materials. Previous developments have contributed to the discovery of different types of new functional materials with

dielectric,[54] magnetic,[55] superconducting,[56] and luminescent properties.[57] In this section, I will talk about how does plasma sputtering work and why we apply this tool on our research. Also, a detailed introduction of the film preparation will be concluded in the methodology chapter.

1.3.1 Plasma and Townsend Discharge

Named by Irving Langmuir in 1929, plasma usually means the ionized gases containing a series of species including electrons, ions, and neutral atomics etc. With the specific properties it has, plasma has been described as the "Forth State" which distincts from solid, liquid, and gas.[58] In the case of sputtering, plasma has been applied as the source for the ionized species to bombard the surface of the target to deposit thin film and this starts with Townsend Discharge.

At the beginning, the gas inside the chamber is insulating gases like Ar. The dielectric breakdown process starts with a high voltage between the metal electrodes. With electric field applied, an electron near the cathode is traveling toward anode carrying a current i_0. With increasing speed and kinetic energy, the electron eventually will accumulate sufficient energy to collide with a neutral gas atom and coverts it into a positively charged ion. This charge conservation process will generate two electrons and one positively charged ion:

$$e^- + A \rightarrow 2e^- + A^+ \tag{1.10}$$

Those two electrons will go through the same process and release two additional positively charged ions and four electrons. With this chain reaction going on, the electric field applied will keep pulling the ionized ions toward cathode and pushing the current carrying electron toward anode. The ions will collide with the cathode and will be ejected back to the gas cloud, colliding with other species and creating secondary electrons. This process will snowball until a sufficient large current make the gas breakdown. John Sealy Townsend conclude this process with Townsend equation:

$$i = i_0 \frac{\exp \alpha d}{[1 - \gamma_e(\exp \alpha d - 1)]} \tag{1.11}$$

Here i is the discharge current, i_0 is the initial current given by the voltage to the electron, and γ_e is the Townsend secondary-electron emission coefficient that defined as the number of secondary electrons emitted at cathode per incident ion. d is the distance between the electrodes. It must be long enough to allow electrons to accumulate energy and to ionize atoms. At the same time the electrodes also need to be wide to block the electrons from traveling out of the interelectrode space. α is the probability of ionization occurring per unit length which related to charge of the electron q and traveling distance λ:

$$\alpha = \frac{1}{\lambda} exp^{-\frac{V_i}{q\varepsilon\lambda}} \tag{1.12}$$

The breakdown will happen when $\gamma_e(\exp \alpha d - 1) = 1$ in equation 1.11. That means the current is infinite after breakdown. On the other hand, the breakdown voltage V_B, can be related with discharge pressure in Paschen's Law:

$$V_B = A \frac{P \cdot d}{\ln(P \cdot d) + B} \tag{1.12}$$

Here, A and B are both constant. When the pressure is too low, there would not have enough electron-ion collision happening, and the secondary electron yield will be too low to maintain the chain reaction. If the pressure is too high, the collision will be too frequent; the mean free path of the secondary electrons will be small that those electrons do not have enough energy to ionize the atoms. Thus, the discharge will be quenched.[53]

1.3.2 Magnetron Sputtering

The magnetron sputtering applies magnetrons to help decrease the operation voltage and pressure while increasing the deposition rate.[53] The magnet is usually concealed underneath the

target of the gun. With the application of both the electrostatic force and Lorentz force, the electrons will stay within the interelectrode area and accumulate more kinetic between collision. This allows the discharge to happen in relatively low voltage and low pressure. The low pressure allows the sputtered atoms to fly off and impinge on substrate with minimum collision and scattering with the plasma cloud which will randomize the traveling direction and lower the deposition rate. As shown in Figure 3(a), under the effect of combinational magnetic field and electric field, the energetic ions will have more interaction with the cathode/target, and this will lead to a dense plasma in the near cathode area. Figure 3(b) shows the dense ring glow above the target during the plasma sputtering. This will eventually form a erode ring on the surface of the target where the plasma is most intense.

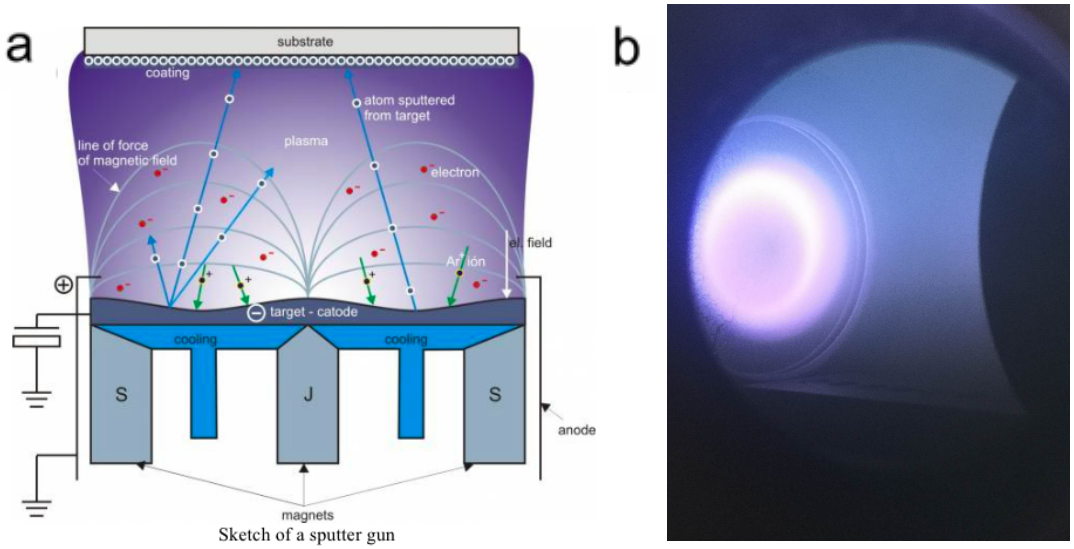

Figure 1.3 *(a)The scheme of a magnetron plasma gun.*[59] *(b) Plasma glow above target during plasma sputtering*

1.3.3 DC and RF Sputtering

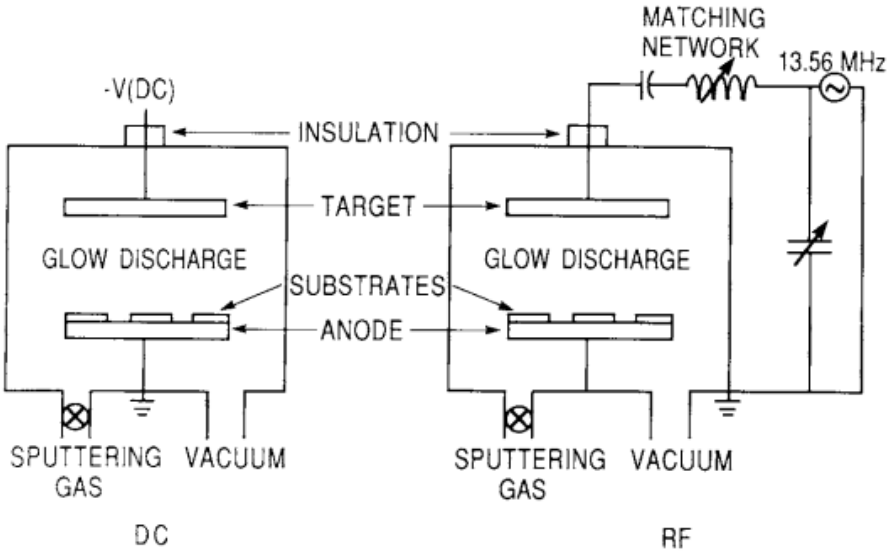

Figure 1.4 *Scheme of DC and RF sputtering system*[53]

There are two types of sputtering applied in our experiment; direct current (DC) and radio frequency (RF). The main difference between those two approaches is the difference of their power source. DC sputtering use DC power while RF use AC power source.

The mechanism of DC has been illustrated in the earlier section, and the scheme of both systems is shown by Figure 4. The discussion about DC here is the factors influence deposition rate. At low pressure, the collision happens less frequently, and the mean free path is large. The ions are ionized far from the target and the chance for them to traverse outside the interelectrode area is great. Less ion-impact-inducted secondary electrons will be created. Therefore, the self-sustain discharge is hard to maintain due to low ionization efficiency. On the other hand, if the pressure is too high, the collision frequency between the sputtered atoms and the species in the plasma cloud will dramatically increase and lead to collisional scattering. This will lead to decrease in deposition rate as well. An equation has been used to relate deposition rate and some important factors[60]:

$$\dot{G} \approx \frac{\bar{\mathscr{p}}_d < x_{th} >}{g\rho(1+\gamma_e)E} \tag{1.13}$$

Where $\bar{\mathscr{p}}_d$ is the discharge power-density (W/cm^2), $< x_{th} >$ is the mean distance from the cathode that sputtered atoms could travel before they get thermalized, g is the interelectrode distance, ρ is the atomic density (atoms/cm^3), γ_e is the Townsend secondary-electron emission coefficient and E is the average sputtering energy. Therefore, at fix pressure and cathode voltage, deposition rate is directly related with the applied power while inversely related with interelectrode distance. [53]

The main concern about DC sputtering is the arc on the surface of the target where charge easily accumulate when the target is poorly electric conductive. At most of the time, the thin oxide layer on the metal target surface will be quick removed after the sputtering process starts. Arcing won't be an issue in that case. But for the case of oxides or other types of insulators, arcing damage and pollute both substrate and target. Also, the film structure will be altered, and defect will form. [61,62] Therefore, for oxide, semiconductor and insulator (ρ>10^6 Ω-cm) deposition, RF will be a better choice.

1 MHz is a rough board line between high frequency for RF sputtering. [63] The frequency is regulated by Federal Communication Commission (FCC) through Industrial, Scientific and Medical (I.S.M.) radio band to avoid harmonic oscillate between the plasma generator and other devices. The frequency is set to be 13.56 MHz [64]. The discharge mechanism of RF is similar with DC glow discharge, yet the electrons oscillate in the glow region and then traveling to the sheath region when the AC oscillate. Sheath region is a dark region in front of the cathode where only a portion of the electron is energized enough to ionize the atoms while other low energy electrons collide with the atoms without ionization. The discharge voltage among this region is low. Because of the AC fluctuation, the pulsating plasma sheath reflect the electrons back and forth between the

glow and sheath. During the process, electrons returning to glow from sheath will gain additional energy from the simultaneously expanding sheath region. The consequence for this series of interaction make the discharge sustain easier that cathode secondary electrons are no longer necessary to maintain the discharge. As mentioned previously, the biggest advantage for RF is the capability to sputter high resistivity materials because voltage can be coupled through any kinds of impedance and allows current to pass through.

The deposition rate of RF is slower than DC because the AC power source with lower voltage and the lack of secondary electrons above cathode. However, due to the limitation of the tools and power source, Pd-TM alloys are sputtered by the RF while a Titanium underlayer is deposit through DC.

To better control the morphology and crystallinity, a RF bias is applied to the substrate. Applying RF bias on the substrate enhances the positive charged ion bombardment in the negative half-cycle. This ion-cleaning process is believed to be effective to remove the impurity adsorbates and hydro-carbon remnant on the surface of the substrate. Applying substrate bias can improve adhesion in the initial stage of the film forming, increase in purity because of the continuous ion cleaning process, and crystallinity due to more ordered atom arrangement during bombardment. [53,65]

1.4 High Throughput Screen Methodology

Because it is challenging to analyze the reaction products and assess the catalytic activity over a small region on a large catalyst library. Previous screen methods of solid-state heterogenous catalysts are relatively low efficient.

Over the past two decades, a number of researchers redirected their focus to improve the methodology to screen fuel cell catalysts. Mallouk et al. reported on a fluorescent acid-base

indicator technique to detect the concentration of proton, which is generated during the methanol oxidation and screened a broad range of binary, ternary and quaternary precious metal catalysts with an optimal composition of $Pt_{44}Ru_{41}Os_{10}Ir_5$.[66] Hillier et al. proposed scanning electrochemical microscopy (SECM) as a reliable technique for screening PtRu-based catalysts for the hydrogen or methanol oxidation.[6768] Bard et al. designed the piezo-based microarray dispenser to prepare catalyst arrays for a wide range of M-Co bimetallic alloys (M: Pd, Ag, Au) and reported Pd-Co (10-30% Co) exhibited the optimal activity for the ORR in acidic media using SECM.[69] Also, previous work of Abruña group employed the fluorescent-based method to screen Pt-M binary alloys (M included 18 elements in the periodic table) and selected promising catalysts, such as $Pt_{65}Ru_{35}$. Their composition, structure and fiber texturing were characterized by synchrotron-based X-ray fluorescence and diffraction. [70,71,72]

The rotation disk electrode (RDE) system has been widely used as standard tools to evaluate catalyst activity/durability of fuel cell electrocatalysts. At the same time, the fluorescent based and SECM techniques only provide indirect predication of the ultimate activity. Those results are needed to be translated into realistic activities in RDE measurements for catalyst screening. Here, I am reporting a facile catalyst screening method using replaceable glassy carbon disk electrodes as the substrate, which enables the rapid and reliable evaluation of ORR activity under RDE measurements. A high-throughput magnetron sputtering is used to prepare binary Pd-M alloy (M: Mn, Fe, Co, Ni and Cu) electrocatalysts for the ORR in alkaline fuel cells. Among about 40 kinds of binary alloys, Pd-Cu (ratio 1:1) is examined to be the most promising candidate. Guided by this result, a parallel research project about PdCu nanoparticles using impregnation-reduction method is being operated by Abruña group.

2. Methodology

The combinational screening methodology utilize magnetron sputtering as high throughput fabrication method for sample preparation. XRD and SEM-EDS have been used for standard structure, morphology and composition characterization. RDE is applied as the direct measurement for catalytic activity under alkaline environment.

2.1 Magnetron Plasma Sputtering

Compare to nanoparticle synthesis, sputtering can create a quality alloy thin film with composition gradient from 0~100% within a short period of time. The sputtering system used in this work is a customized RF sputtering system built by UHV instrument in 1980s named "Fenris" (Figure 2.1).

2.1.1 "Fenris" RF Magnetron Plasma Sputtering System

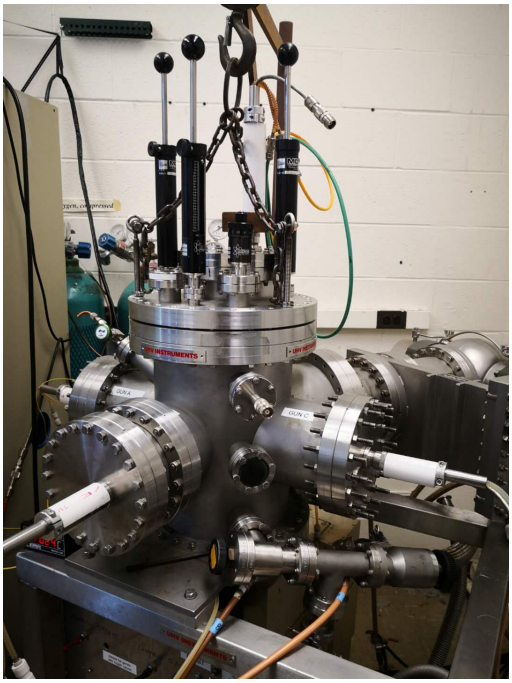

Figure 2.1 *Picture of Fenris*

Fenris is an instrument designed for non-conductive materials (insulator, semiconductor etc.) sputtering. It is connected to oxygen, nitrogen and argon gas tanks, and has the capability to perform reactive sputtering. Even though not idea, Fenris can be used for metal/alloy sputtering as well. The problem is the relatively slow deposition rate compare to DC, yet this does not have big influence toward this project. The reason why Fenris is used as the main tool is because other chambers are either down with malfunction or need inspection. Fenris is the only chamber up for operation during the period of this project.

Fenris have totally four 2-inc sputtering guns. Three off-axis guns connected with RF power source is on the same plane with the substrate holder. One new installed top gun connected with DC power source is on-axis facing substrate from the top lid. Two guns along x direction (Gun A and Gun C) and the top gun have been used in this project. The layout is shown on Figure 2.2 where two guns heading against each other in the opposite direction to create composition gradient of the alloy.

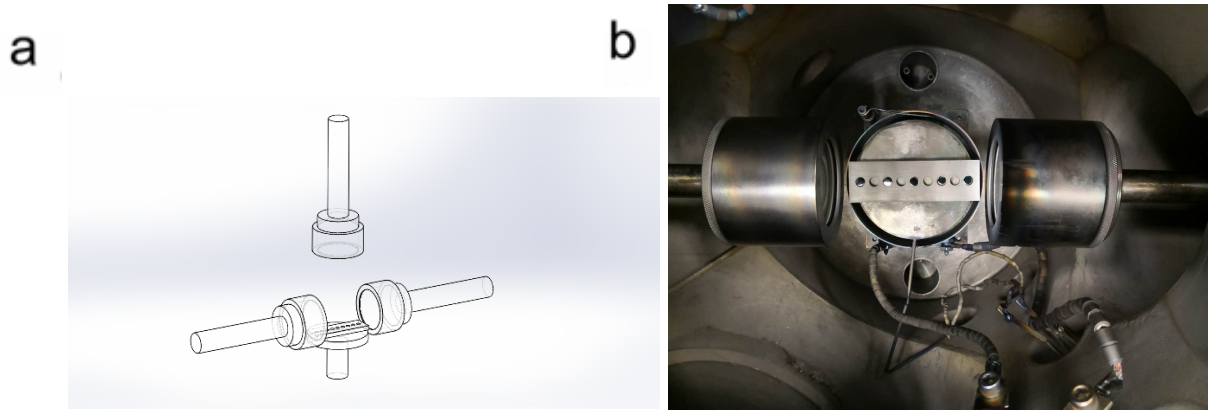

Figure 2.2 ***The layout of Fenris (a) CAD sketch of Fenris with two sputter guns on the side for preparing Pd-M binary thin films and one Ti gun on the top for sputtering adhesion layer. (b) Picture taken inside the chamber showing the home-made ceramic sample holder with glassy carbon electrode between the two sputter guns (Pd and 3d metals).***

During the sputtering process, both RF source guns are pushing toward the substrate holders yet being kept about 0.5 inches from the substrate. Gun A (the gun on the left-hand side

on Figure 2.2 (b)) is installed with Palladium while Gun C (the gun on the right on Figure 2.2 (b)) is installed with other transition metals (Cu, Co, Mn, Ni etc.). Because the substrate is glassy carbon which has poor adhesion of the film. The top gun is set to be on-axis to sputter a uniform thin Titanium adhesive underlayer before the Pd-M alloy is sputtered. Each gun has a manual shutter which will be closed during the pre-sputter/surface ion clean process. During the sputtering process, the shutter will open. The substrate holder stage is connected to a RF bias to improve both adhesion and the film quality.

The chamber is connected to a UHV instrument mechanical pump which pumps the chamber down to intermediate base pressure around 50~100 mtorr where turbo pump can be safely turned on. This process will take about 5-8 minutes. Then the turbo pump on the back of the chamber will bring the base pressure down to the 10^{-7} torr range in 8-10 hours. The mechanical pump connected to the chamber is also working as the backup pump of the turbo pump to further pump out the gas inside the turbo pump.

2.1.2 Deposition rate calibration

Before the sputter process, calibration is a vital step needs to be done to set up the parameter for sputter process. Since this study requires good composition gradient spread where the 50% should be in the center spot of the substrate, knowing the deposition rate of both metals becomes critical. The calibration is done by black wax lifting and profilometer is used to measure the thickness of the film.

The first step is to draw a line on silicon wafer with black wax horizontally across the center. Then install the wanted metal on one of the off-axis guns and put the silicon wafer in to set up the chamber. Deposit the metal we want to calibrate, mind the length of the time it takes for the

sputtering, wash the black wax off with trichlor solution, and then measure the thickness of the film under profilometer (Figure 2.3).

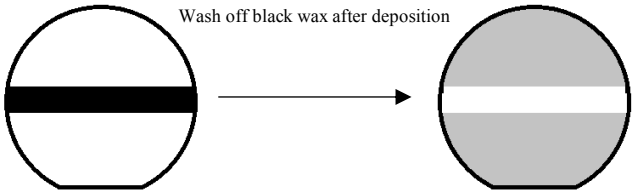

Figure 2.3 *Black wax application process*

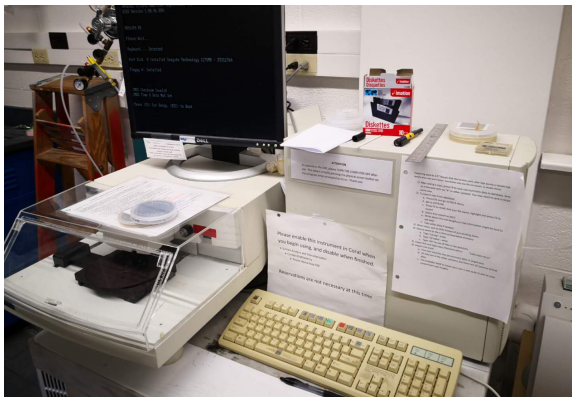

Figure 2.4 *Tencor AlphaStep 500 stylus profilometer*

As shown on Figure 2.4, the stylus profilometer provided by Cornell Center for Materials Research (CCMR) is a Tencor AlphaStep 500 model. It is a tool to generate a line-scan topographical profile of the sample surface. The vertical resolution is 1 Å with a 13 μm range or 25 Å with a 300 μm range. [73] The Profilometer uses a stylus to touch the surface of the sample and runs across edge between the channel left by black wax lifting and the film. The difference the stylus measures is the thickness of the film. For the purpose of finding the deposition rate, I measure the thickness around the center of the sample. From there, the thickness of the film divided by the time it takes to deposit is the deposition rate of the material.

2.1.3 Glassy Carbon Substrate

For the sake of high throughput screening process and later RDE characterization, the substrates of the thin film are set to be glassy carbons (GC) electrodes. The GC electrode is purchased from HTW GmbH (Germany). The GC rod is cut into columns (D = 5mm, H = 5 mm) and one side is mirror polished and thoroughly cleaned with ethanol and H_2O (Figure 2.5(a)). A ceramic electrode holder is custom built to hold up to 9 GC electrodes per batch for co-sputtering of binary alloys (Figure 2.5(b)). Those substrates are labeled No.1 to No.9 from the positions near Pd targets (left hand side in Figure 2.5(b)) to those near 3d metal targets (right).

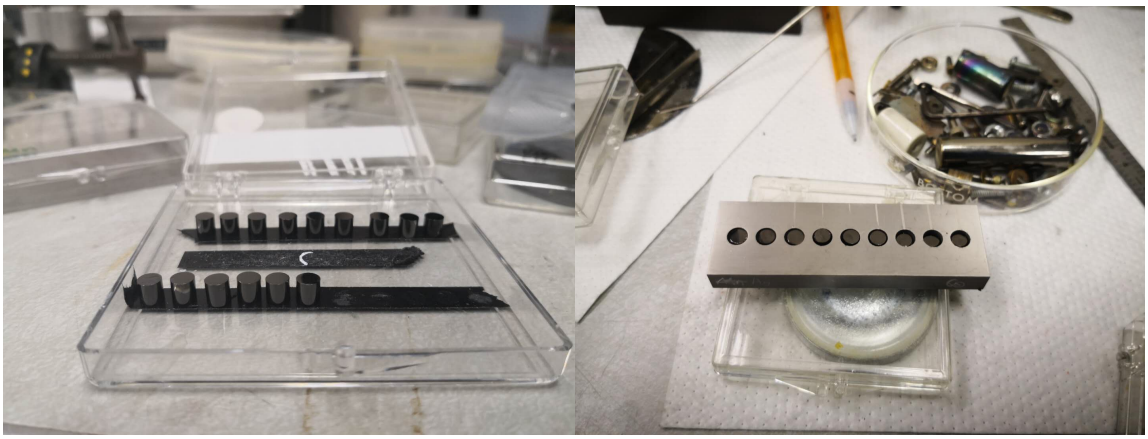

(a) (b)

Figure 2.5 (a) Glassy Carbon substrate (b) ceramic substrate holder with nine GC substrates installed

2.1.4 Operation Procedure

The sputtering process starts with pumping down the chamber. When the chamber reaches the ultimate high vacuum (UHV) condition (~$2E^{-6}$ torr), the environment is ready for sputtering process. Then turn on the gas valve to let the Ar gas flow in at a rate of 40 SCCM. The operating pressure is set to be 30 mtorr.

Through the calibration process, sputter Palladium at 25W will give a deposition rate at 2.5 Å/s. From there, for every Pd-TM alloy we fabricate, the deposition rate for the other alloy metal is set to 2.5 Å/s as well. The detailed parameter is shown on the table below:

Table 2.1 The power for each metal to have 2.5 Å/s deposition rate on Fenris RF guns

	Pd	Co	Cu	Fe	Mn	Ni
Power for 2.5 Å/s	25W	50W	35W	60W	56W	50W

The top on-axis gun deposits a Ti adhesion layer due to the poor adhesive capability of carbon. The parameter for the Ti underlayer is set to be 0.5A with 250V and 125W. The length for deposition is one minute. The expected thickness is 70 nm and the deposition rate is 11.1 Å/s.

Before the sputtering process, the shutters of the guns are closed for ion-cleaning process for the target called pre-sputtering. This process uses ion bombardment to clean off the surface of the target by sputtering off the impurities. With substrate RF bias applied, the surface of the substrate will also be cleaned by ion-bombardment. This process is been used to increase the adhesive capability and the film quality. This is set to run for approximately 3 minutes.

For the sputtering process, the parameters are shown below:

Table 2.2 *The operation parameter of the sputtering process*

Run#	Gun A (RF)	Gun C (RF)	RF Bias	Base Air (Sccm)	Pressure (torr)	Time (Minute)	Expected Thickness (nm)
Pd-Cu	Pd	Cu	7W	Ar 40	2.00E-06	10	400
Power	25W	35W					
Pd-Co	Pd	Co					
Power	25W	50W					
Pd-Mn	Pd	Mn					
Power	25W	56W					
Pd-Ni	Pd	Ni					
Power	25W	50W					

Pd-Fe	Pd	Fe
Power	25W	60W

Besides the power of the gun, every other parameter is set to be identical as controlled variables.

2.2 XRD

X-ray Diffraction is one of the prolific tools to acquire information about the crystallinity and atomic structure of the materials.

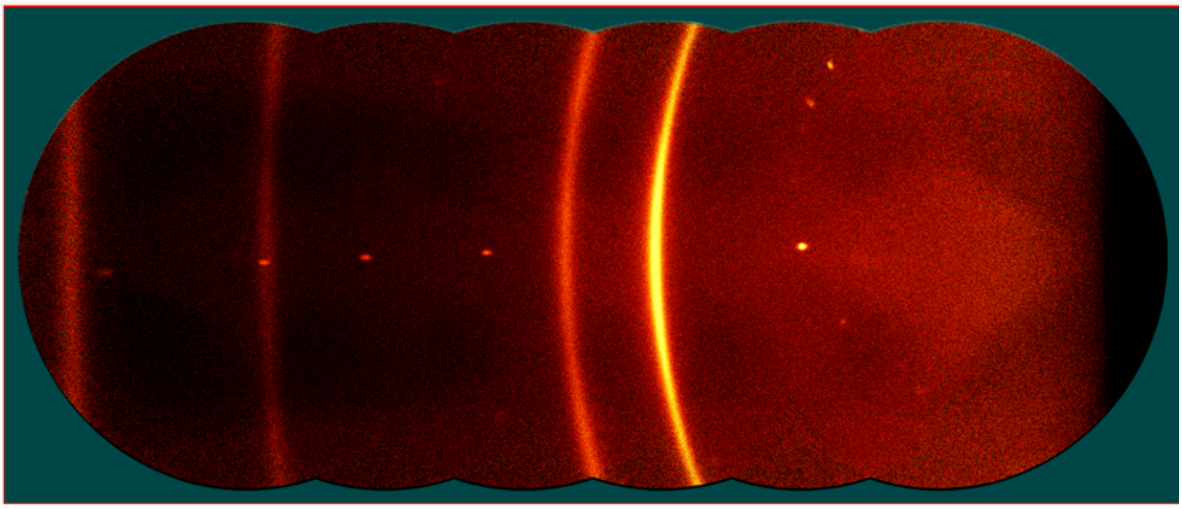

Figure 2.6 *An example of a Pd-Ni XRD pattern acquired from GADDS*

The thin-film XRD patterns are acquired using Bruker D8 General Area Detector Diffraction System (GADDS) with a Vanter 2D large-area detector (Figure 2.7). This system uses collimated Cu-kα (λ = 1.54059 nm) X-ray source. Ni filter is available to eliminate the k-beta radiation.[74] The Vanter area detector of the system detects diffraction perpendicular to the direction of the scattered X-ray beam, and form patterns based on the measured intensities along the diffraction arcs (Figure 2.5).

Diffraction patterns are collected at a step size of 10° /frame and an acquisition time of 1 min/frame. Angle between the X-ray source and the horizon (angle θ) is set to be 15 ° while the angle between the center of the area detector and the direction of the incoming X-ray beam (angle 2θ) moves from 20° to 70°. The area detector itself covers an area of approximately 30°. This makes the 2θ axis scale on the integration pattern extends from 5° to 85°.

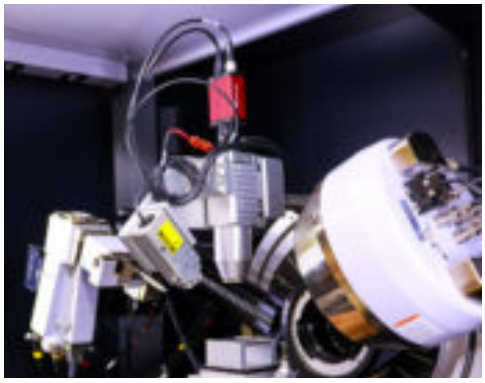

Figure 2.7 ***Bruker GADDS***[74]

To set up, a laser pointer will guide the sample height alignment precisely to ensure the reproducibility among different batches of thin films. The stage is controlled by software and motor which allows the stage to move in both X and Y directions. This enables the position adjustment and detection for multiple spot on a single silicon wafer due to the difference in composition. Since the GC electrode have large diffraction peaks of graphite in the background, Pd-based thin films are deposited on the single-crystal 2inch Si wafer for XRD analysis.

2.3 SEM-EDS

Scanning electron microscopy (SEM) and energy dispersive spectroscopy (EDS) are the popular combinational tools for almost all kinds of scientific research. SEM shoots electrons toward the sample and collects the secondary electrons scattered from the surface of the materials to reveal the morphology of the sample. When the electrons bombard the sample and secondary

electrons get ionized and jumping out, some lower energy states have been empty while some electrons from the outer orbitals transit to the lower energy state and emit X-ray. EDS collects the X-ray emitted from the sample and separates the characteristic X-ray into an energy spectrum. The purpose of using SEM-EDS is to find the composition of the sample across the horizontal axis and the morphology under different composition.

SEM images capture and EDS are performed using ZEISS Gemini 500 SEM (Figure 2.7) provided by CCMR. Films are sent to the instrument on top of the glassy carbon substrates. SEM images are acquired at 3 kV and 1 nA. EDS spectrums are acquired at 20kV and 38 nA to maximize the X-ray signal output for elemental quantification while maintain reasonable spatial resolution for elemental mapping. EDS spectrum image is obtained with a size of 256×256 pixels and a dwell time of 2.5 ms/pixel. EDS elemental mapping of Pd and 3d metals are processed using Pd Lα,β and 3d metal Kα edges in ImageJ.

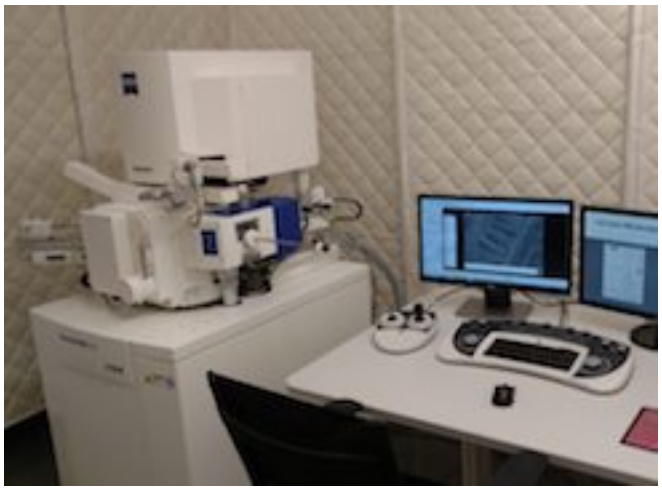

Figure 2.8 *Zeiss Gemini 500 SEM-EDS*[75]

2.4 RDE

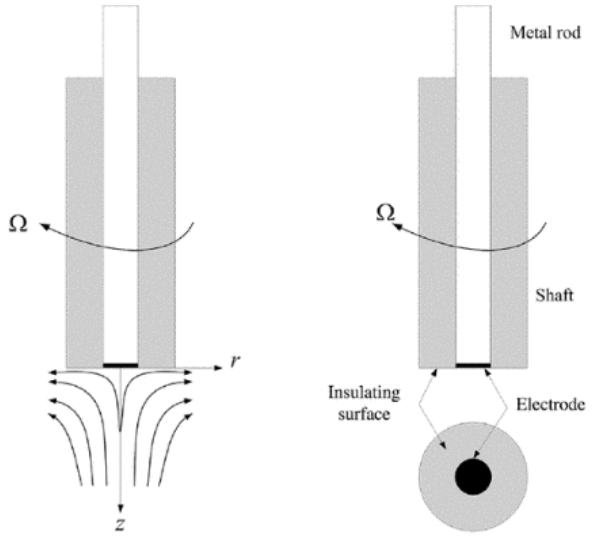

Figure 2.9 *Rotating Disk Electrode*[76]

As a prolific high throughput characterization method, RDE has been widely applied to characterize the catalytic activity of fuel cell catalyst. Figure 2.9 shows the structure scheme of an RDE system where an electrode is imbedded in the end of a cylinder connected with motor. The electrode will be submerged and rotate in the electrolyte. The reasons why RDE has drawn a lot of attention are because the hydrodynamics is well known, steady mass transfer rate, and rather simple construction. [76] What's more, as mentioned previously, RDE gives direct profile about the catalytic activity. Those factors make RDE an important part in our methodology.

The basic steady state analysis has been comprehensively modelled by von Karman and Cochran. The velocity profiles are:

$$v_y = -0.51\omega^{\frac{3}{2}}v^{-\frac{1}{2}}y^2 \tag{2.1}$$

And

$$v_r = 0.51\omega^{\frac{3}{2}}v^{-\frac{1}{2}}ry \tag{2.2}$$

v_y is the normal fluid velocity, v_r is the radial fluid velocity. y is the vertical distance and r is the horizontal radius. ω is the angular velocity. v is the kinetic viscosity. At surface the rotating disk spin with the electrolyte fluid at an angular speed where both the v_r component and v_y component are zero. Away from the surface, the centrifugal force velocity v_r. In the vertical direction toward the bulk where $y \to \infty$, v_r is zero and v_y is at a limiting velocity. Then, for limit current steady state convective-diffusion equation[76]:

$$v_y \left(\frac{\partial C_o}{\partial y}\right) = D_0 \frac{\partial^2 C_o}{\partial y^2} \tag{2.3}$$

And substitute in equation (2.1)

$$-0.51\omega^{\frac{3}{2}} v^{-\frac{1}{2}} y^2 \left(\frac{\partial C_o}{\partial y}\right) = D_0 \frac{\partial^2 C_o}{\partial y^2} \tag{2.4}$$

Here, the left-hand side term of equation (2.3) stands for convection and the right hand side stands for diffusion. D_o is diffusivity and C_o is concentration.

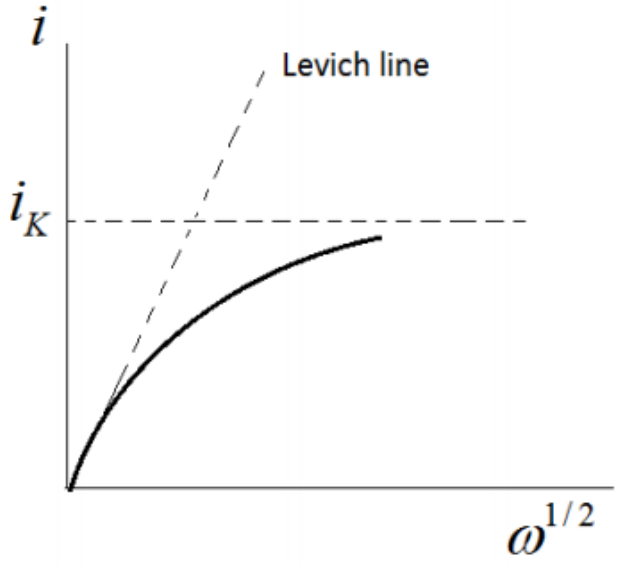

Figure 2.10 *Variation of i with $\omega^{\frac{1}{2}}$ at an RDE for an electrode with slow kinetics*[77]

Current is the flux at electrode surface:

$$i = nFAD_o \left(\frac{\partial C_o}{\partial y}\right)_{y=0} \tag{2.5}$$

While the current density is uniform across the surface and mass transfer is controlling, the Levich equation:

$$i_d = 0.62nFAD_o^{2/3}\omega^{\frac{1}{2}}v^{-\frac{1}{6}}C_o^* \tag{2.6}$$

Here n is the electron transfer number and C_o^* is the bulk concentration of the electrolyte. From Levich equation, i_d is expected to have linear relation with $\omega^{\frac{1}{2}}$ (Figure 2.1). However, with sluggish reactions, the relationship deviates from the straight line. There is, yet, intrinsic kinetic of reaction involved in the current output. The Levich equation is rearranged into Koutecky-Levich equation:

$$\frac{1}{i} = \frac{1}{i_K} + \frac{1}{i_d} = \frac{1}{i_K} + \frac{1}{0.62nFAD_o^{\frac{2}{3}}\omega^{\frac{1}{2}}v^{-\frac{1}{6}}C_o^*} \tag{2.7}$$

$$i_K = nFAk_f(E)C_o^* \tag{2.8}$$

The $k_f(E)$ is the reaction rate at E (V). The result is plotted on Figure 2.11. Therefore, the slope for both lines is $(0.62nFAD_o^{\frac{2}{3}}v^{-\frac{1}{6}}C_o^*)^{-1/2}$. $\frac{1}{i_K}$ is the intercept where i_K is the kinetic current. Also, different lines represent different potentials. The intercept value exhibits the current density in the absence of any mass-transfer limitations. From there, the parameters inside the slope, like diffusivity D_0 and n the electron transfer number.

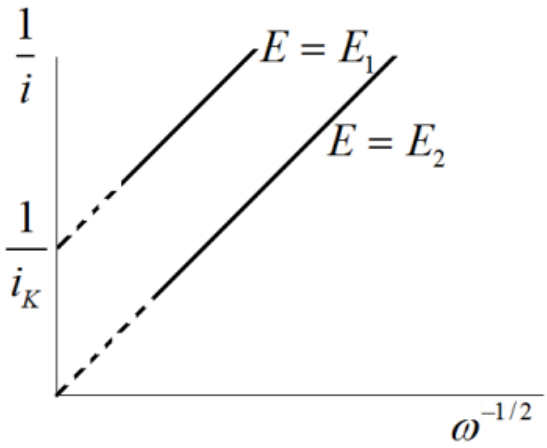

Figure 2.11 *Koutecky-Levich plots at potential E1, where the rate of the electron transfer is sluggish to act as a limit factor and E2, where electron transfer process is quick.*[77]

A replaceable disk electrode (Pine Instrument, E4TQ) is employed as the standard RDE platform for evaluating the ORR activity of Pd-based thin films. The thin film coated GC working electrode (WE) is loaded into the electrode holder (2.12) with Teflon tape on the side for tight sealing to prevent electrolyte leaking. The GC in holder is pushed against the internal Au spring-loaded pin to ensure a reliable electrical contact.

Figure 2.12 *RDE setup*

Ag/AgCl in saturated KCl solution served as the reference electrode (RE) and connected to the WE through a salt bridge. A large-surface-area graphite rod is used as the counter electrode (CE). The potential difference between Ag/AgCl in saturated KCl and a reversible hydrogen electrode (RHE) in 1M KOH is calculated to be 1.0258 V based on the Nernst equation. Electrochemical measurements are performed on a Solartron potentiostat. ORR measurements are carried out in oxygen-saturated 1M KOH solution at 1600 rpm and 5 mV/s room temperature (23 ^{o}C). The relative activity is calculated by normalizing the kinetic current, extracted from the Koutecky-Levich equation, to the relative Pd contents of Pd in the binary alloys. Cyclic voltammogram (CV) profiles are obtained in Ar-sat. 1M KOH at a scan rate of 10 mV/s.

3. Result and Discussion

As mentioned previously in the methodology chapter. The samples are prepared through magnetron sputtering deposition, and then characterized by SEM-EDS, XRD, and RDE to find the optimal composition for Alkaline ORR catalytic activity. We have been looking into 7 different combinations: Pd-Cu, Pd-Co, Pd-Ni, Pd-Ni, and Pd-Mn. Among them, Pd-Cu and Pd-Co show promising characteristics in electrocatalytic activity. Pd_{50}-Cu_{50} is the best among the others while Pd_{80}-Co_{20} also shows decent catalytic activity, which is the best among Pd-Co alloys.

3.1 SEM-EDS

SEM-EDS is an important part of the methodology to investigate the surface morphology and chemical composition of the thin films. We have use SEM-EDS to investigate the composition over Pd-Cu, Pd-Co, Pd-Fe etc. The surface morphologies show good uniformity and the composition spread of the materials are steady and similar. Those are the proof of high film quality from magnetron sputtering.

3.1.1 Pd-Cu

Figure 3.1 (a) and (b) exhibit the result from binary magnetron sputtering and EDS. As shown in Figure 3.1 (a), the composition of Cu shows progressive change from position 1 to position 9 while Pd shows a same trend in the opposite direction. The Pd $L_{\alpha,\beta}$ edges at around 2.8 keV shows a gradual decrease in the intensity while the Cu $K_{\alpha,\beta}$ edges at 8.0 and 8.9 keV became stronger, suggesting the Pd at.% decreases while Cu at.% increase from the sample position 1 to position 9. Ti K_{α} edge at 4.5 keV is also detected due to the Ti adhesion layer under Pd-Cu films. The relative Pd at.% and Cu at.% are quantified based on the Pd L and Cu K edges using the Cliff-Lorimer equation[78]

The total elemental contents of Pd and Cu at.% are set to 100% and the relative errors (one standard deviation) are estimated to be 1-2%. As shown in Figure 3.1 (b), the Pd composition smoothly decreases from 95% in sample position 1 to only 5% in sample position 9. With the sputtering powers of Pd and Cu targets calibrated, $Pd_{50}Cu_{50}$ (Pd/Co atomic ratio, 1:1) can be achieved in the position 5, which is the center point between to guns. It is estimated the composition change by about 1.3 at% for each 1 mm on the sample. For a GC electrode with a diameter of 5mm, one would expect a composition variation of 6.5% across one GC. The compositions reporte here are the values at the center of all GC electrodes.

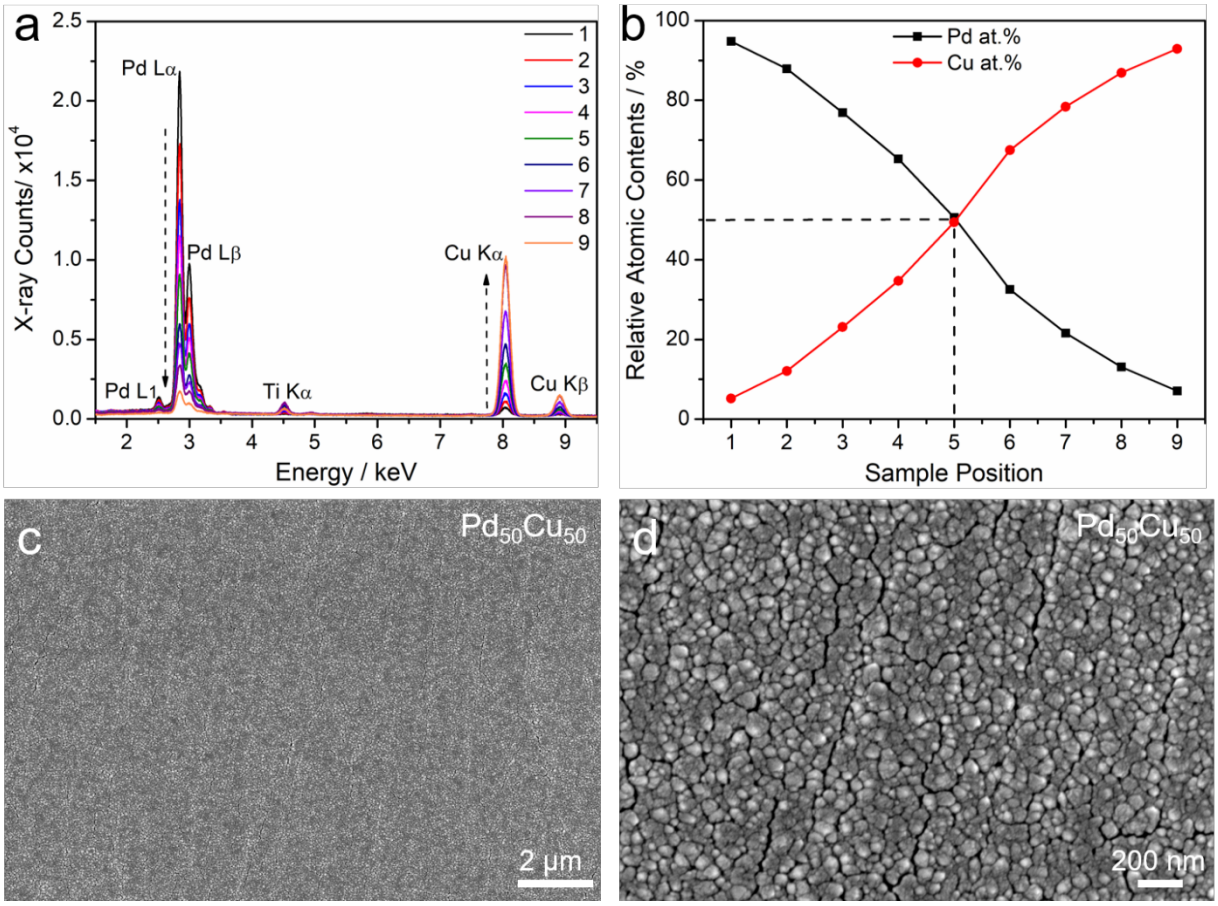

Figure 3.1 ***Elemental quantification of Pd-Cu thin-film electrodes. (a) EDS spectra of Pd-Cu thin films with sample position from 1 to 9 (Pd-rich to Cu-rich). Pd Lα,β and Cu Kα edges are used for elemental quantification. Ti signal came from the Ti adhesion layer. (b) Relative atomic contents of Pd and Cu (at.%) as a function of sample position, which covers the range of Pd at.% from ~95% to ~5% and $Pd_{50}Cu_{50}$ in position 5 (c and d) SEM images of $Pd_{50}Cu_{50}$ showing a uniform film morphology and a domain size of around 100 nm.***

SEM is used to characterize the morphology of the thin films. $Pd_{50}Cu_{50}$ is used as an example to demonstrate the homogeneity of sputtered thin films (Figure 3.1 (c)). Over the field of view of 16 µm or larger, $Pd_{50}Cu_{50}$ shows good uniformity with no noticeable µm-sized agglomeration. The magnified SEM image of $Pd_{50}Cu_{50}$ in Figure 3.1(d) suggests that the smooth surface is composed of metal clusters with a size of around 100 nm. The surface morphology of Pd-rich and Cu-rich films are also examined under SEM (Figure 3.2). Both $Pd_{77}Cu_{23}$ and $Pd_{22}Cu_{78}$ (estimated as Pd_3Cu and $PdCu_3$) thin films exhibit highly homogenous surface morphology over the µm-sized field of view. (Figures 3.2 (a), (c)). When compared to $Pd_{50}Cu_{50}$, $Pd_{77}Cu_{23}$ shows similar surface morphology with clusters around 100nm (Figure 3.2 (b)). $Pd_{22}Cu_{78}$ shows a smoother surface morphology, possibly due to the relatively higher mobility of Cu atoms comparing to Pd atoms, during sputtering (Figure 3.2 (d)).

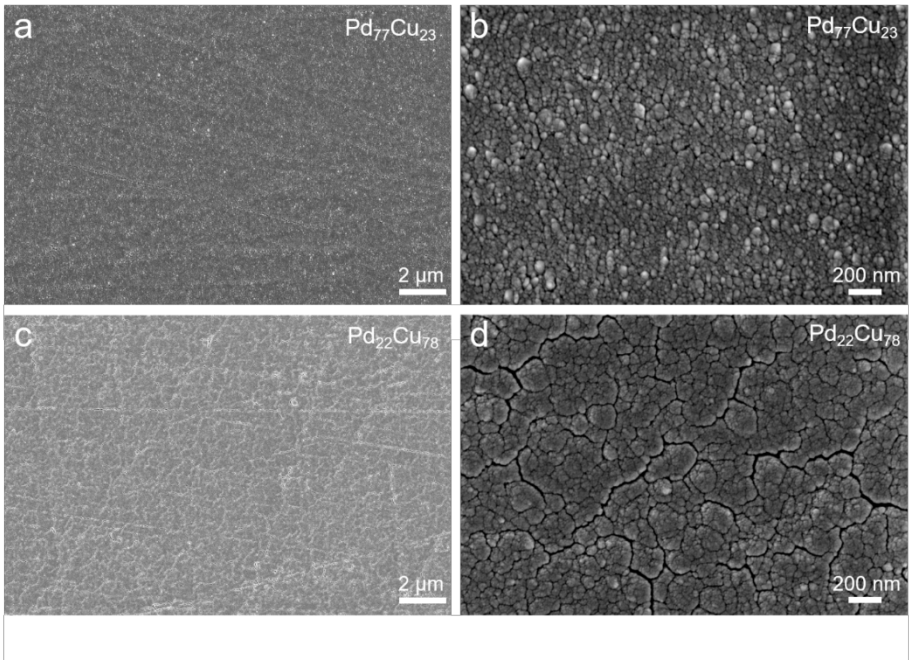

Figure 3.2 *(a) and (b) SEM images of Pd-rich $Pd_{77}Cu_{23}$ under 2 µm magnification and 200 nm magnification. (c) and (d) are Cu-rich $Pd_{22}Cu_{78}$ thin films under the same magnification respectively. (b) shows the domain size of around 100 nm on the surface of $Pd_{77}Cu_{23}$. The surface of $Pd_{22}Cu_{78}$ tends to be smoother than $Pd_{77}Cu_{23}$.*

After examining the surface morphology and bulk compositions, it is important to know the structure and chemical composition on the cross section of thin films on the substrate. The SEM image in Figure 3.3 and 3.4 presents the cross section of a $Pd_{50}Cu_{50}$ thin film on top of the Ti adhesion layer on the glassy carbon substrate. Since the image intensity is not sensitive to the atomic number of elements, EDS mapping is employed to evaluate the elemental distribution on the cross-section areas. The L edge of Pd and K edges of C, Ti and Cu are used to form EDS elemental maps. The EDS maps of C, Ti, Pd and Cu provide a direct visualization of the layered structure of PdCu/Ti/GC along the cross section (Figures 3.3 and 3.4 (b-e)). In particular, the EDS map of Ti suggests a Ti adhesion layer with a thickness of around 50 nm (Figure 3.3 (c) and 3.4 (c)). The EDS maps of Pd and Cu indicate a catalyst layer of around 350 nm (Figures 3.3 (d-e) and 3.4 (d-e)). The composite map of Pd vs. Cu in Figures 3.3 (f) and 3.4 (f) show a relatively homogenous elemental distribution of Pd and Cu, indicating the successful formation of binary alloys at the nanometer scale. Two mappings are done on the same sample yet different location to confirm that the thickness is identical and minimize the error.

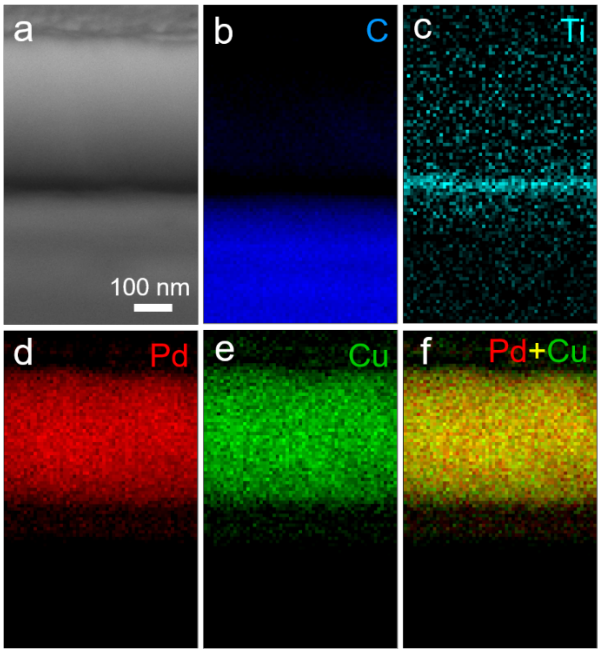

Figure 3.3. *SEM image (a) and the corresponding EDS elemental maps of (b) C, (c) Ti , (d) Pd, (e) Cu and the composite map (f) of Pd vs. Cu. The thickness of Pd-Cu thin films and Ti underlayer are estimated to be 350 nm and 50 nm, respectively. The uniform false color map in yellow in (f) suggests the relatively homogenous elemental distribution of Pd and Cu.*

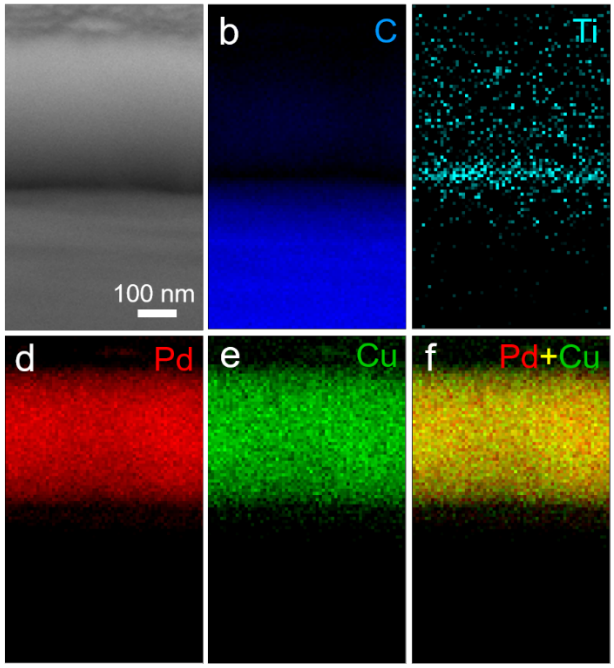

Figure 3.4 *Another SEM sample image (a) and the corresponding EDS elemental maps of (b) C, (c) Ti , (d) Pd, (e) Cu and the composite map (f) of Pd vs. Cu. The thickness of Pd-Cu thin films and Ti underlayer are estimated to be 350 nm and 50 nm, respectively. The uniform false color map in yellow in (f) suggests the relatively homogenous elemental distribution of Pd and Cu.*

3.1.2 Pd-Co

Figure 3.5 (a) presents the EDS spectra of Pd-Co thin films with Ti as the adhesion layer. The intensity is normalized to Co K_α edges to better show the changes in Pd at.%. Pd-Co thin films shows decreasing intensity trend of Pd from position 1 to position 9, which is similar to Pd-Cu.

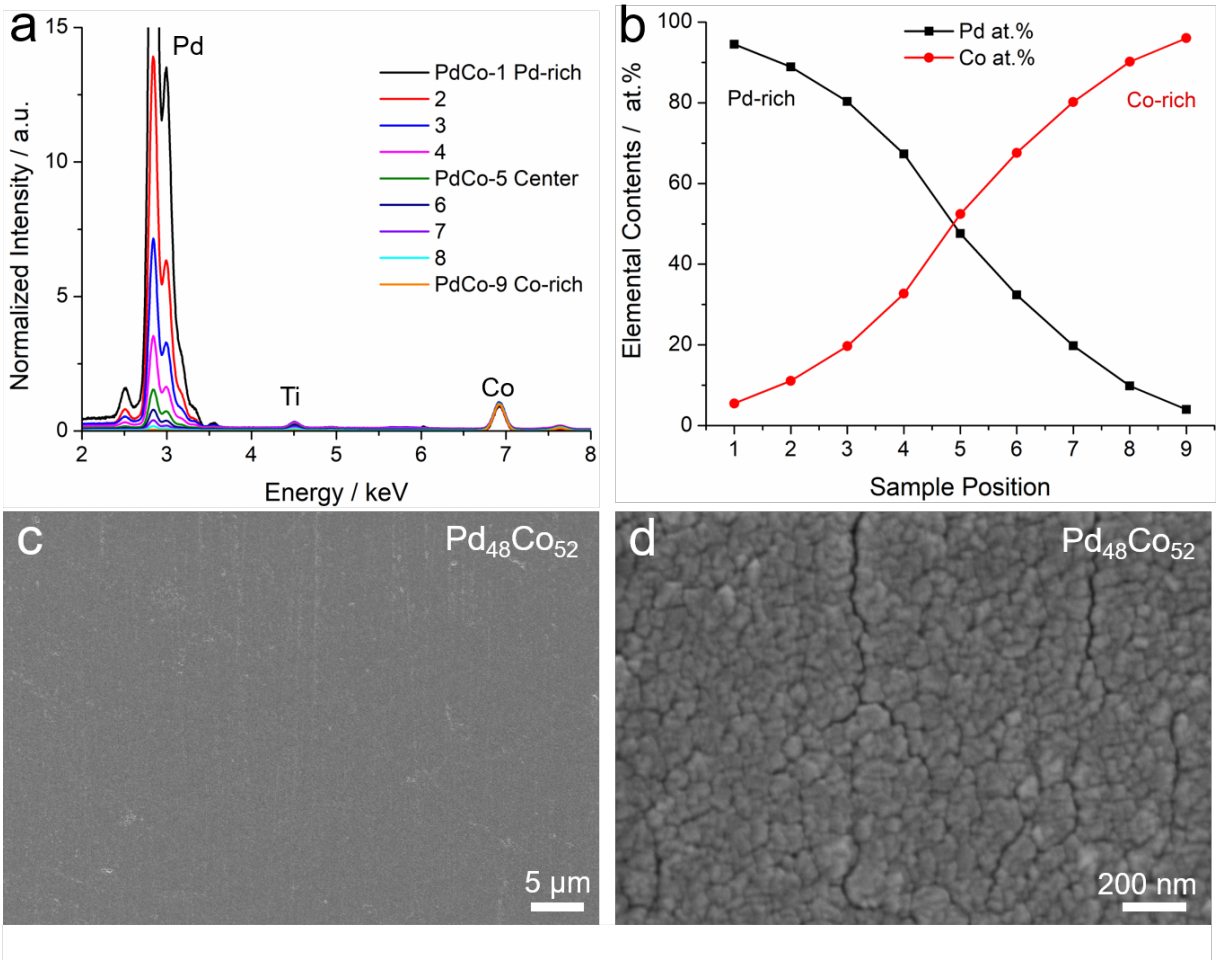

Figure 3.5 ***Elemental quantification of Pd-Co thin-film electrodes. (a) EDX spectra of Pd-Co thin films with sample position from 1 to 9 (Pd-rich to Co-rich). Pd Lα, β and Co Kα edges are used for elemental quantification. (b) Relative atomic contents of Pd and Co (at.%) as a function of sample position, which covers the range of Pd at.% from ~95% to ~5% and $Pd_{50}Co_{50}$ in position 5 (c) and (d) SEM images of $Pd_{50}Co_{50}$ showing a uniform film morphology and a domain size of around 100 nm.***

As shown in Figure 3.3 (b), the composition of Pd at.% decreases from 95% in position 1, to 48% in position 5 in the middle and finally to 5% in position 9. SEM images of $Pd_{48}Co_{52}$ exhibits a highly uniform surface morphology (Figure 3.3 (c)) and metal clusters with sizes of around 100 nm (Figure 3.3 (d)).

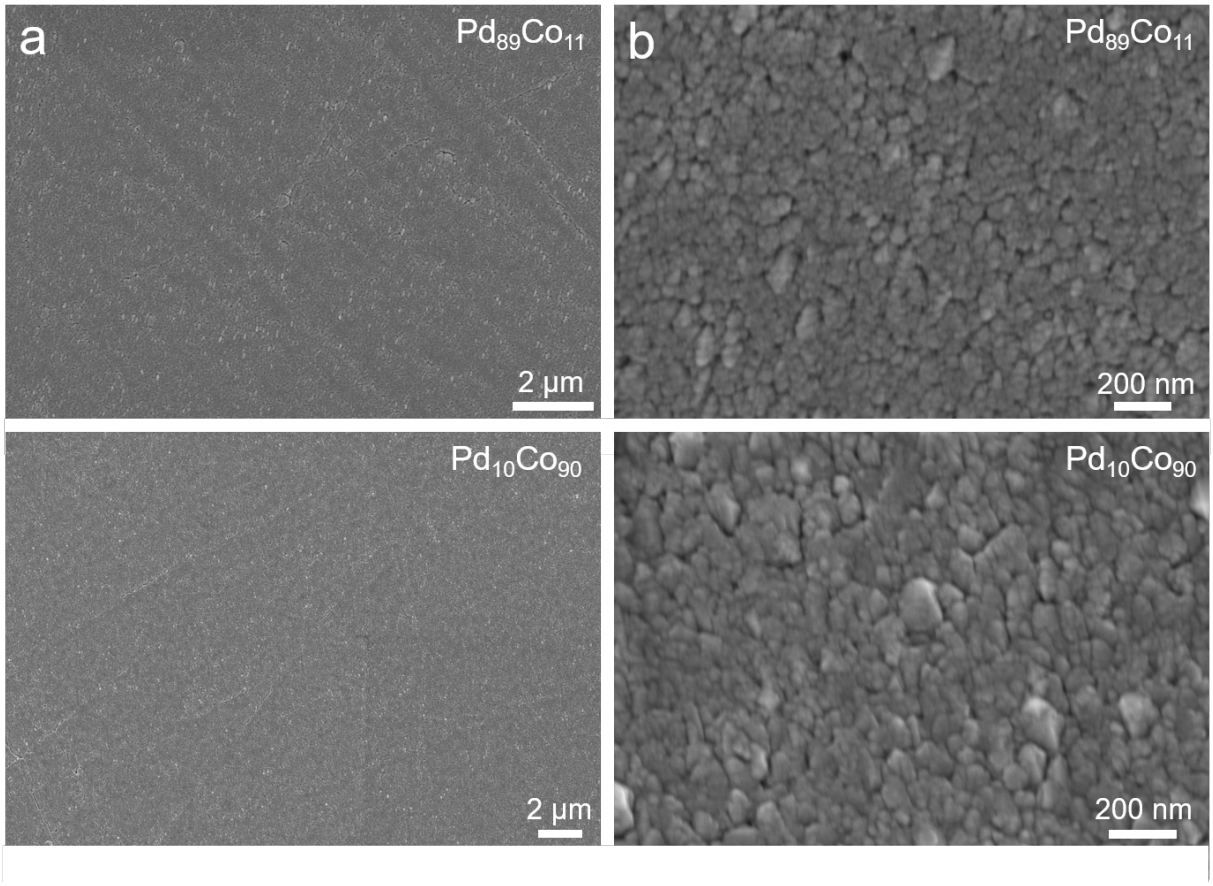

Figure 3.6 *(a-b) and (c-d): SEM images of Pd-rich $Pd_{80}Co_{11}$ and Cu-rich $Pd_{10}Co_{90}$ thin films, respectively, showing the uniform film morphology and domain size of around 100 nm.*

Pd-rich and Co-rich films (e.g., $Pd_{89}Co_{11}$ and $Pd_{10}Co_{90}$) also show the similar homogenous morphology as well as the nm-sized metal clusters (Figure 3.4). Compare to $Pd_{50}Co_{50}$, the surface morphology of $Pd_{89}Co_{11}$ and $Pd_{10}Co_{90}$ are slightly rougher due to the existence of the clusters.

3.1.3 Others

Pd-Cu and Pd-Co are the most detailed analyzed combinations since they show decent catalytic activity in RDE. SEM image for others are not taken, yet EDS has been performed for Pd-Ni and Pd-Fe. Those materials also exhibit similar regular patterns in the composition variation from Pd-rich composition in sample position 1 to the 3d metal-rich composition in position 9, with $Pd_{55}Ni_{45}$ or $Pd_{48}Fe_{52}$ in sample No.5.

3.1.4 Conclusion

In summary, four families of Pd-based binary thin films (Pd-Cu, Co, Ni and Fe) are examined to have well-controlled compositions. Pd-Cu and Pd-Co are proved to have uniform surface morphology. EDS quantification suggests that Pd-based thin films are able to cover the entire composition range from 95% to 5% with a step size of around 10% among nine continuous GC substrates. SEM images of selected samples indicate that Pd-based thin films are highly homogenous in the surface morphology and exhibit metal cluster with sizes of around 100 nm.

3.2 XRD

As introduced before, XRD has been employed to characterize the crystal structure of the samples. The XRD patterns of Pd-based thin films would be introduced following the orders of Pd-Cu, Co, Ni, Fe and Mn. A reference background data has been taken by operating XRD on an empty silicon substrate. The pattern is shown in Figure 3.7.

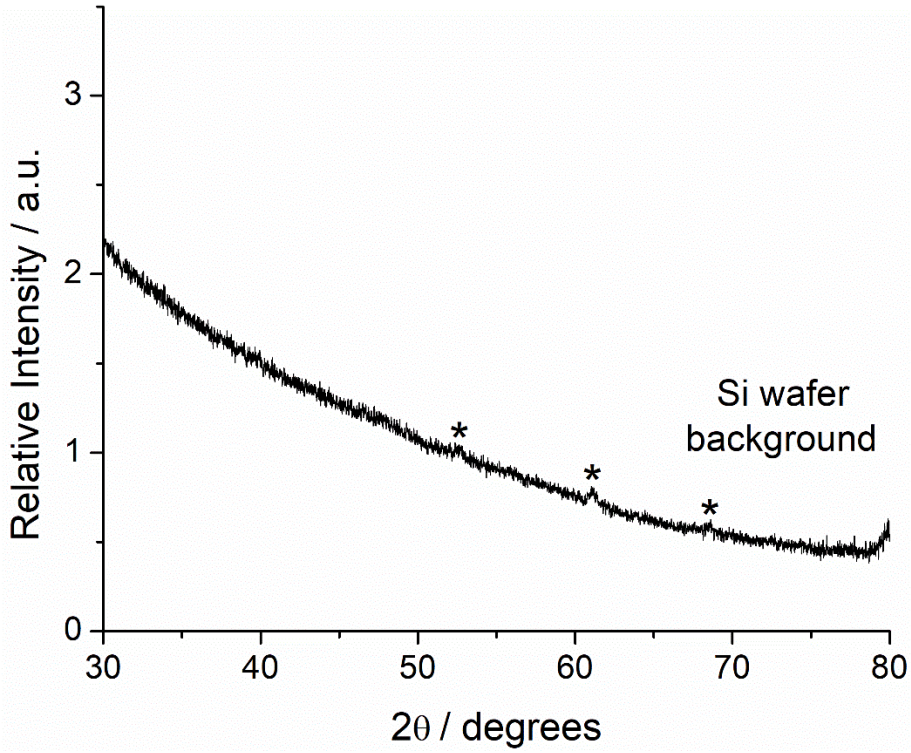

Figure 3.7 ***XRD pattern of the Si wafer. The small peak at around 52, 61, 68 degrees, are ascribed as the background/artifact during the X-ray acquisition using the GADDS instrument.***

3.2.1 Pd-Cu

As shown on Figure 3.8, the nine testing spots of Pd-Cu exhibit single-phase face centered cubic (fcc) solid solutions with the characteristic peaks such as, (111), (200) and (220). As the thin film positions shift from Pd-rich position 1 to Cu-rich position 9, the diffraction peaks, such as (111), also progressively shift to higher angles due to the incorporation of Cu with a smaller atomic size into the Pd lattice. Extra diffraction peaks are examined to origin from the background rather than impurity phase of the binary thin films.

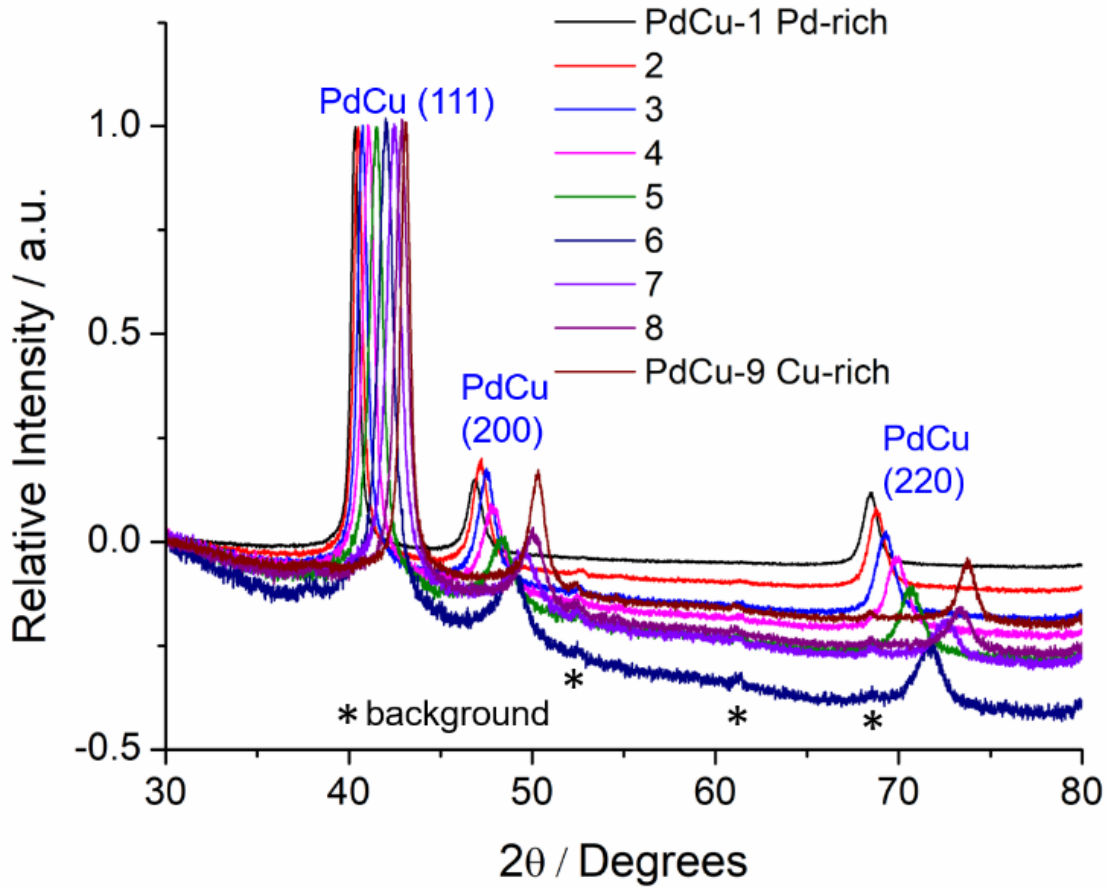

Figure 3.8 *XRD patterns of Pd-Cu thin film with the characteristic (111), (200) and (220) peaks of face centered cubic (fcc) type Pd-Cu binary alloys. The background artifact is labeled as *.*

3.2.2 Pd-Co

As shown on Figure 3.9, Pd-Co also exhibits single-phase fcc solid solutions except that the position 9 (Pd_5Co_{95}) shows a hexagonal close packed (hcp) phase (Figure 3.10). Hcp-Co shares a similar crystal symmetry and atom packing (ABA) to the fcc-Co or fcc-Pd (ABCA), and the major (002) diffraction peak of hcp-Co has almost an identical peak position with the major (111) peak of other positions' fcc-Co.

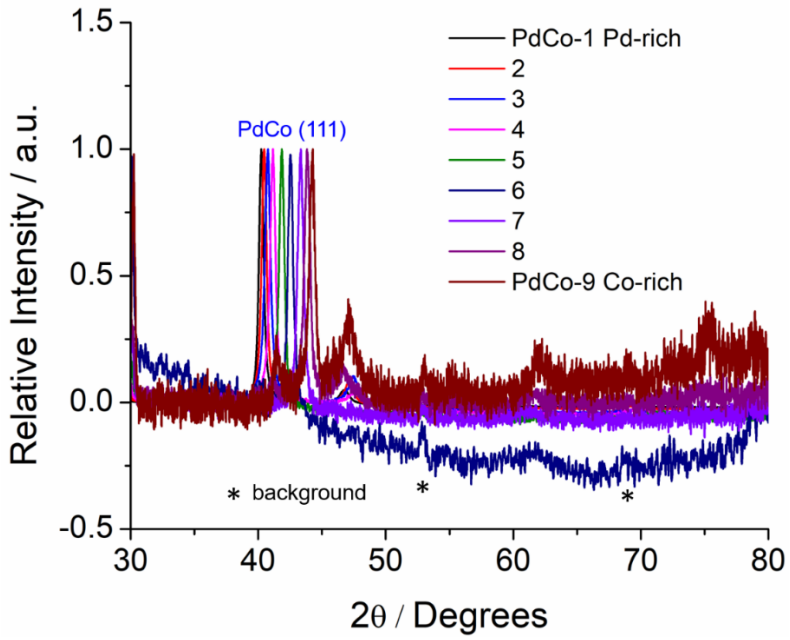

Figure 3.9 *XRD patterns of Pd-Co thin film with the characteristic (111) peaks of face centered cubic (fcc) type Pd-Co binary alloys. The background artifact is labeled as *. Very Co-rich thin film, Pd_5Co_{95}, at position 9, shows the dominant hexagonal centered cubic structure.*

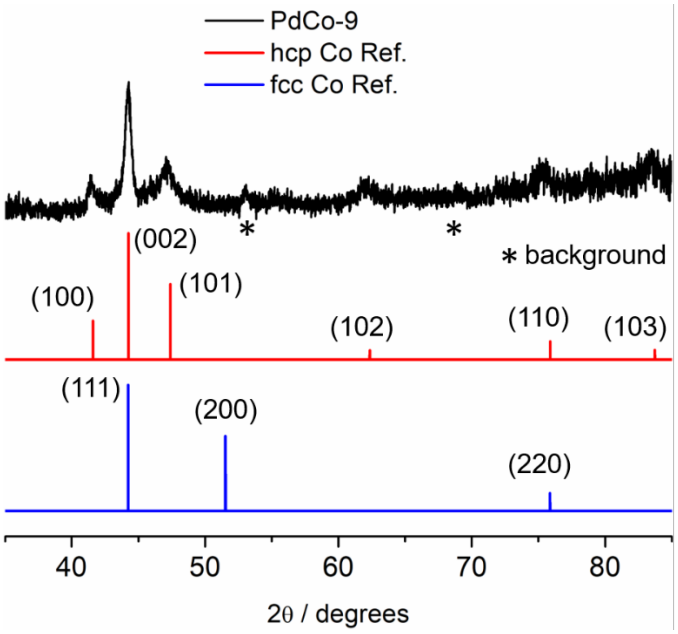

Figure 3.10 Very Co-rich thin film, Pd_5Co_{95} at position 9, shows the dominant hcp cubic structure rather than the fcc structure.

3.2.3 Pd-Ni

As shown on Figure 3.11, Pd-Ni exhibits the similar pattern with Pd-Cu where single-phase fcc solid solutions with the (111) facets gradually shifting to higher angles in more Ni-rich samples.

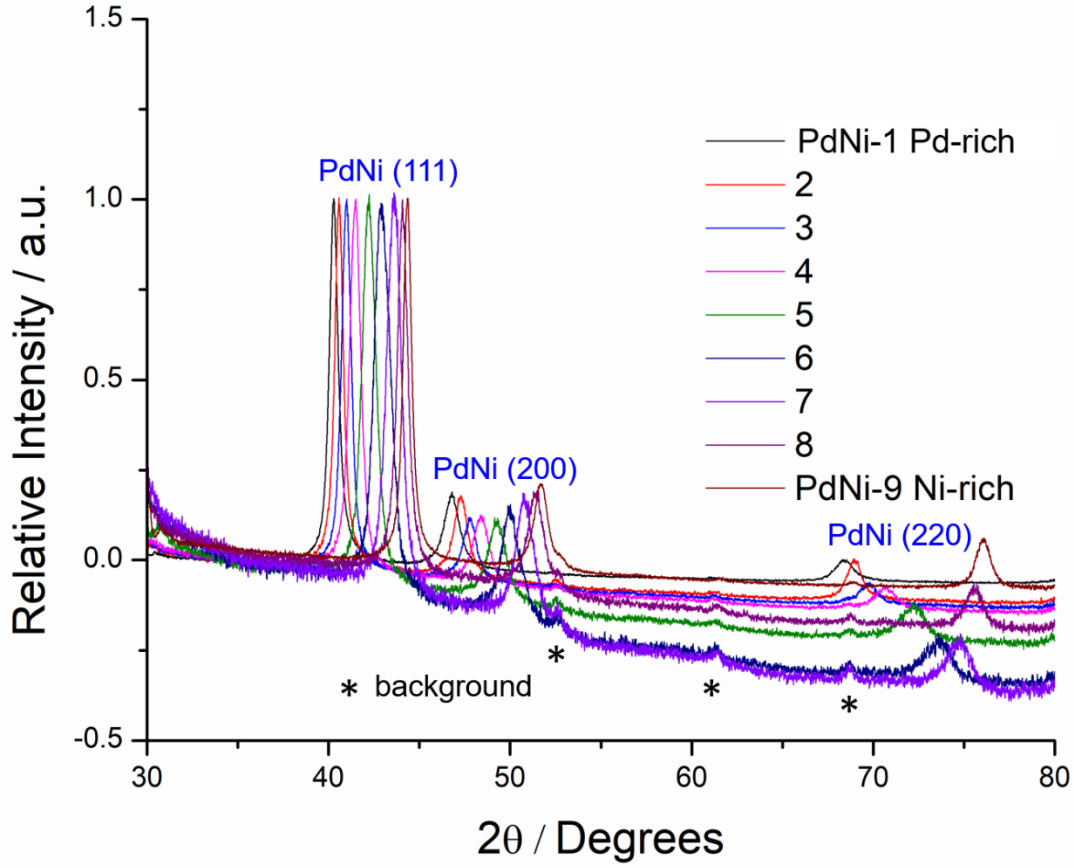

Figure 3.11 *XRD patterns of 9 Pd-Ni thin films with the characteristic (111), (200) and (220) peaks of face centered cubic (fcc) type Pd-Ni binary alloys. The background artifact is labeled as *.*

3.2.4 Pd-Fe

Pd-Fe exhibits more diverse alloy phases as shown on Figure 3.12. It shows different phase then the previous three materials. From Pd-rich position 1 ($Pd_{95}Fe_5$) to position 5 ($Pd_{48}Fe_{52}$), Pd-Fe thin film shows as fcc-phase alloys with (111) and (200) peaks (marked in blue). From position 7 ($Pd_{26}Fe_{74}$) to position 9 (Pd_6Fe_{93}), Pd-Fe thin film are examined to be body centered cubic (bcc)

phase alloys with (110), (200), (220) peaks. It is worth noting that position 6 ($Pd_{31}Fe_{69}$) shows mixed fcc and bcc phases as evidenc by the dominant peak of (111) and a shoulder peak of (110).

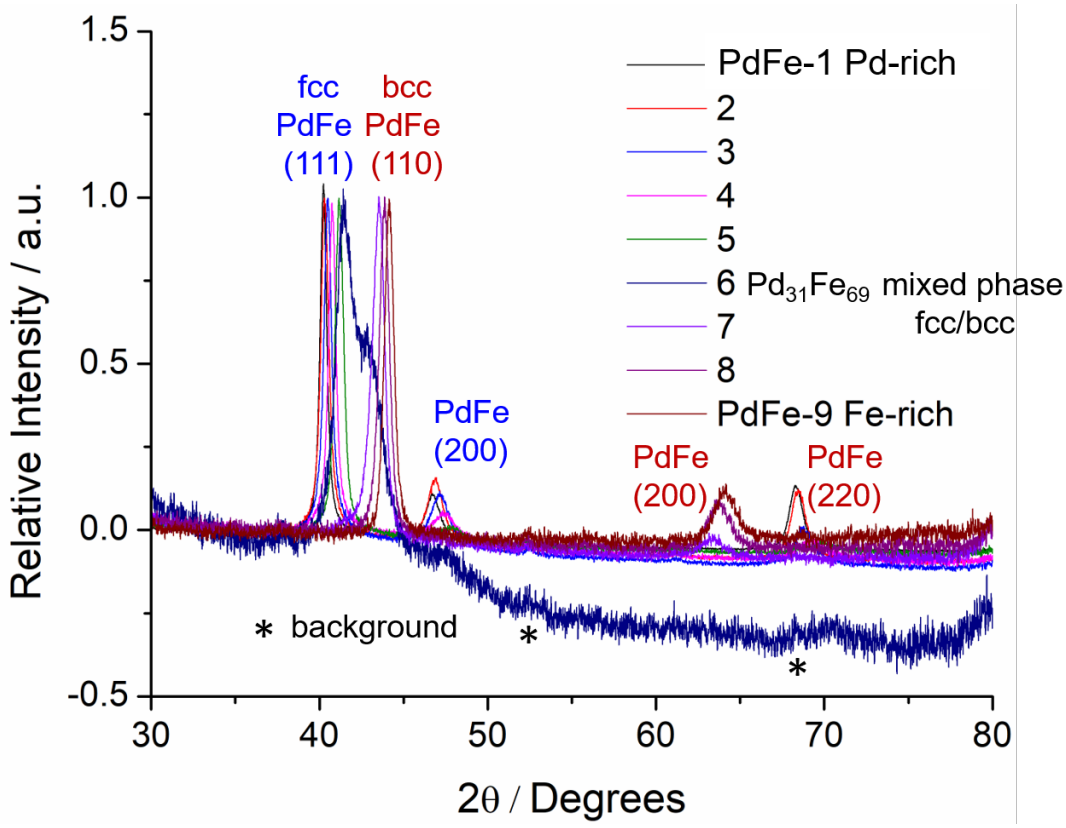

Figure 3.12 *XRD patterns of Pd-Fe thin films. Pd-rich parts of the film (position 1-5) exhibit the fcc structure while the Fe-rich parts (position 7-9) show the body centered cubic (bcc) structure. The position 6 one the film shows the mixed phase of fcc and bcc structures.*

3.2.5 Pd-Mn

Pd-Mn thin film XRD pattern is shown on Figure 3.13. It is a complex situation where mixed phases of fcc-Pd and bcc-Mn across the whole composition range from position 1 to position 9. The peak shift of (111) from position 1 to position 5 is trivial, despite of the dramatic composition changing from $Pd_{95}Mn_5$ to $Pd_{50}Mn_{50}$. This suggests that only little amount of Mn is incorporated into the Pd lattice to cause a noticeable lattice contraction.

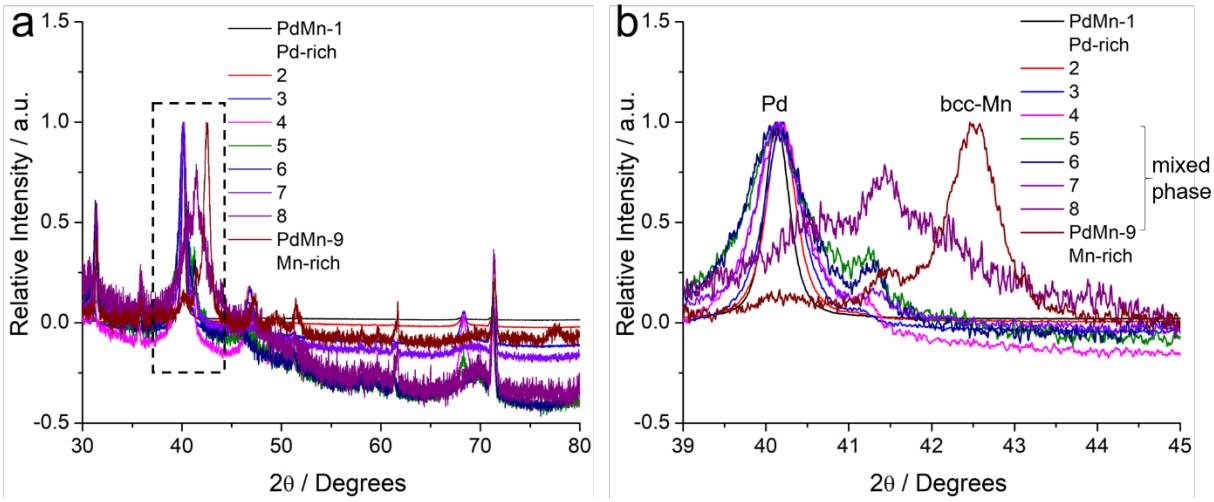

Figure 3.13 *(a) XRD patterns of Pd-Mn thin films. As shown in the magnified region in (b), The (111) peaks at around 40° shows little peak shift despite the composition changes from $Pd_{95}Mn_5$ to $Pd_{50}Mn5_0$, indicating little Mn is incorporated into the Pd lattice. Further increase the Mn contents from $Pd_{50}Mn_{50}$ to Pd_5Mn_{95} results in the mixed phases of bcc-type Mn or Mn-rich alloys with Pd-rich alloys. The XRD patterns suggest that Pd-Mn single-phase binary alloys are not achieved under the current sputtering conditions.*

3.2.6 Conclusion

To quantitatively study the formation of solid solutions between Pd and 3d metals, the major diffraction peak, (111) in fcc phase and (110) in bcc phase are summarized in Figure 3.14 and analyzed using Bragg's law in Figure 3.15. The crystal structures and lattice parameters of Pd and 3d metals are summarized in Table 3.1. The (111) peaks of Pd-Cu and Pd-Ni exhibit obvious trends of shifting to higher angles with increasing at.% of 3d metals (Cu and Ni). $Pd_{50}Cu_{50}$ and $Pd_{50}Ni_{50}$ (green lines) locate right at the middle (Figure 3.14 (a) (b)). Pd-Co thin films exhibits similar patterns except the existence of hcp-Co in very Co-rich sample (Pd_5Co_{95}) (indicated by the arrow in Figure 3.14 (c)). Pd-Fe thin film pattern shows a gradual transition from fcc-type to bcc-type PdFe alloys with the existence of a mixed phase at $Pd_{31}Fe_{69}$ in Figure 3.14 (d). For a solid solution, Vegard's law states that the lattice parameter of a binary alloy will be a weighted average of the two components' lattice parameters at the same temperature[79].

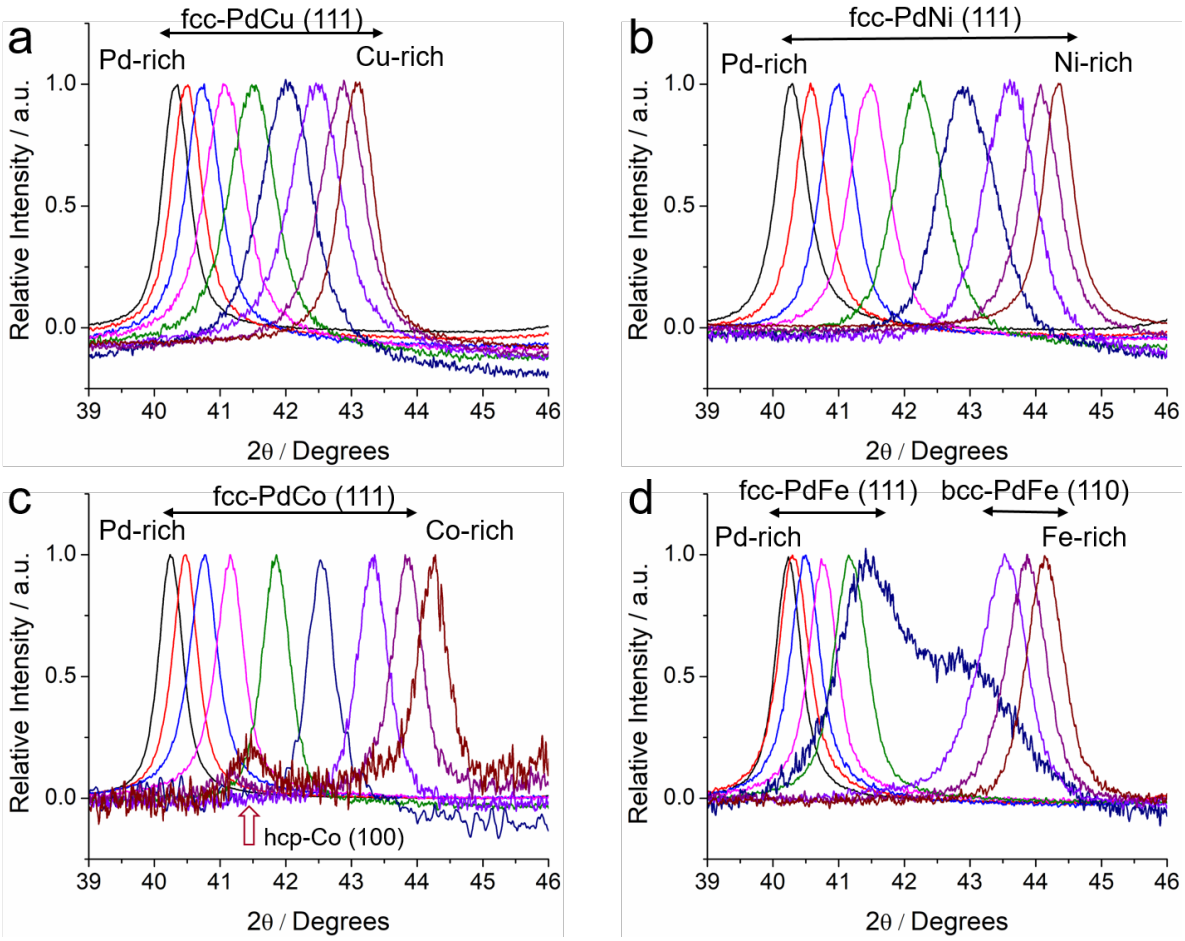

Figure 3.14 ***Summary of XRD patterns of Pd-M binary alloys (M: Cu, Ni, Co and Fe).) XRD patterns of the (111) facets of the 9 positions of (a)Pd-Cu and (b) Pd-Ni thin-film. The composition progressively changed from Pd-rich to Cu-rich or Ni-rich compositions, leading to the gradual peak shift to higher angles due to the incorporation of Cu or Ni atoms with small atomic sizes into the Pd lattice. (c) XRD patterns of Pd-Co thin film, which shows similar patterns as the Pd-Cu and Pd-Ni thin films. The noticeable peak at around 41.5° is ascribed to the formation of hcp-Co at very Co-rich Pd_5Co_{95} film. (d) XRD patterns of Pd-Fe thin films. The first five Pd-rich parts from $Pd_{95}Fe_5$ (black) to $Pd_{50}Fe_{50}$ (green) exhibit a fcc-type PdFe alloys. The Fe-rich part of the film from $Pd_{26}Fe_{74}$ (purple) to Pd_6Fe_{94} (brown) shows the body centered cubic (bcc) structure. The position at $Pd_{31}Fe_{69}$ shows the mixed phase of fcc and bcc structures.***

The lattice parameters of Pd-based thin films are calculated based on the diffraction angles of the major peaks shown Figure 3.14 and plotted as a function of Pd at.% in Figure 3.15. Pd-Cu thin film exhibit a linear relationship between cal. lattice parameter and Pd at.% with a linear fitting coefficient, R^2 at 0.993 (Figure 3.15 (a)). The fitted linear equation is calculated as y=0.0027x + 3.62. The Y-intercept (3.62) at 0% of Pd is consistent with the lattice parameter of pure Cu (3.615 Å). The slope (0.0027) is the percentile difference in the lattice parameter of Pd and Cu ((d_{Pd} +

d_{Cu})/100), which is consistent with the theoretical values of 0.00275. Those results strongly suggest Pd-Cu thin film forms complete solid solution. Pd-Ni exhibits a similar liner relation with a remarkable R^2 value of 0.997. The Y-intercept (3.52) and slope (0.0038) match well with the theoretical values of 3.524 and 0.00366, respectively (Figure 3.15 (b)). Pd-Co shows a reasonably good linear relation with a R^2 value of 0.989 (Figure 3.15(c)). The last point corresponding to the hcp-type Pd_5Co_{95} is a little off from the fitted line, which is possibly due to the difference in lattice parameters between hcp-Co and fcc-Co (Table 3.1). Pd-Fe shows two distinct categories of linear relations in Pd-rich fcc-type alloys and Fe-rich bcc-type alloys (Figure 3.15(d)). Both exhibits a linear relation with R^2 values of ≥ 0.99, and Y-intercepts and slopes matched well with the theoretical values. The formation of bcc-type Fe-rich films (Fe at.% from 74% up to 94%) is possibly ascribed to the significant difference in crystal structures between fcc-type Pd and bcc-type Fe.

Table 3.1 Summary of lattice parameters of Pd and 3d metals. Co and Fe can exist in two phases.

Elements	Pd, fcc	Cu, fcc	Ni, fcc	Co, fcc/hcp	Fe, fcc/bcc	Mn, bcc
Lattice Parameters (Å)	3.890	3.605	3.524	3.544/ a=b=2.505, c=4.089	3.647/ 2.932	3.081

Defining crystal structures and lattice parameters of Pd and 3d metals can help us rationalize the similarity and difference among different families of Pd-M thin films (Table 3.1). In general, in order to form a single-phase solid solution, two components should have same or similar crystal structures and lattice parameters. The relative differences in lattice parameters of Pd and Cu, Pd and Ni are about 6% and 9%, which are moderate to cause lattice contractions yet induce phase segregation.

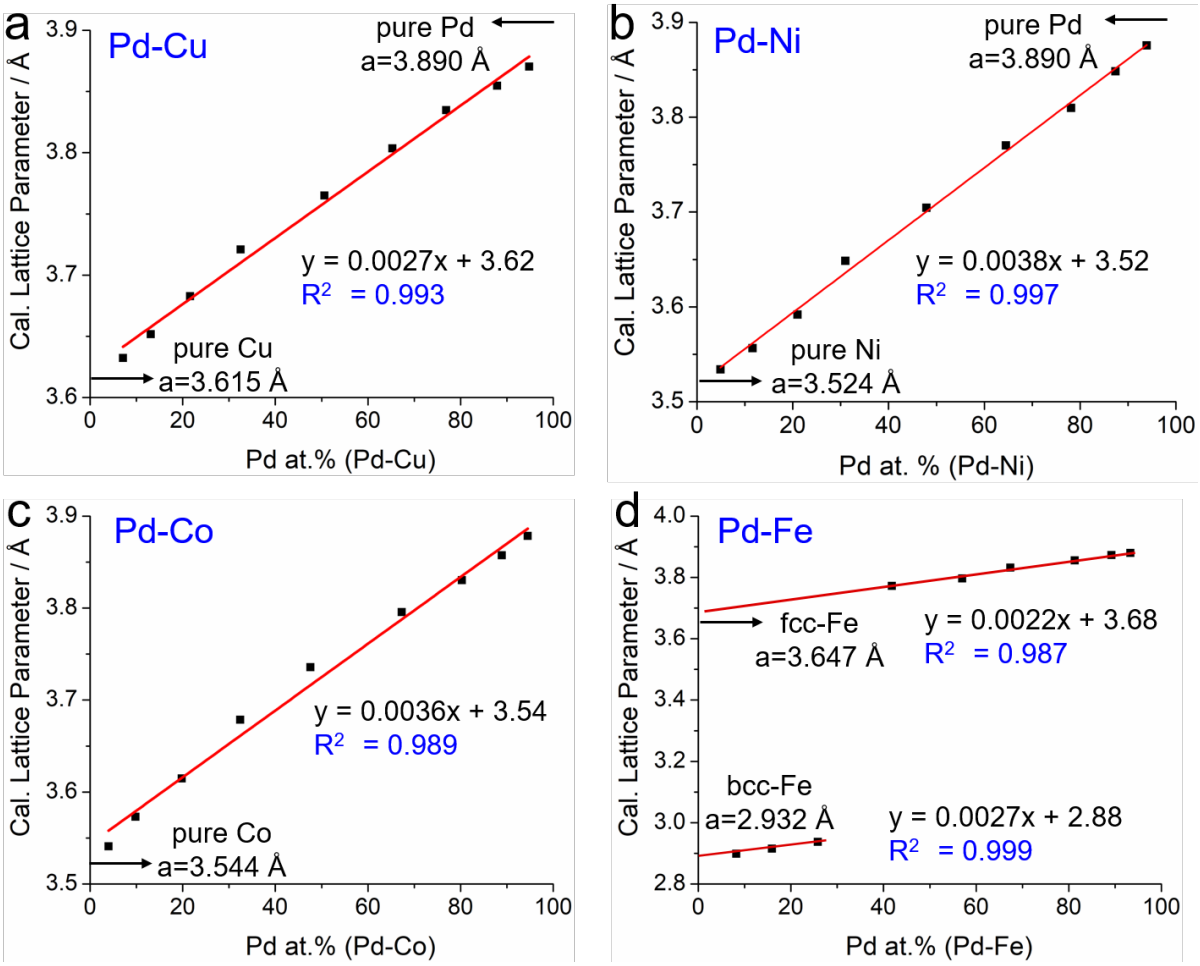

Figure 3.15 ***Linear relation of calculated lattice parameters and relative Pd at.% in Pd-M thin films, following the predication of Vegard's law. (a) The lattice parameter of Pd-Cu thin film calculated from the position (111) peaks as a function of the Pd at.%. The scattered plot is fitted into a linear expression of y = 0.0027x + 3.62 with a high quality of R2 = 0.993. The y-intercept is the lattice parameter of Cu and the slope is the lattice parameter difference between Pd and Cu divided by 100. The lattice parameter of (b) Pd-Ni and (c) Pd-Co thin films as a function of Pd at.%, show good linear relationship. (d) The lattice parameter of Pd-Fe as a function of Pd at.%, which is divided into two regions: the Pd-rich parts (position 1-6) and the Fe-rich regions (samples 7-9).***

The easy formation of Pd-Ni and Pd-Cu solid solutions can also be understood from the phase diagram (Figure 3.16). Despite of some multi-phase regions (white) in the Pd-Cu phase diagram, Pd-Cu still shows a complete solid solution among the whole composition range.

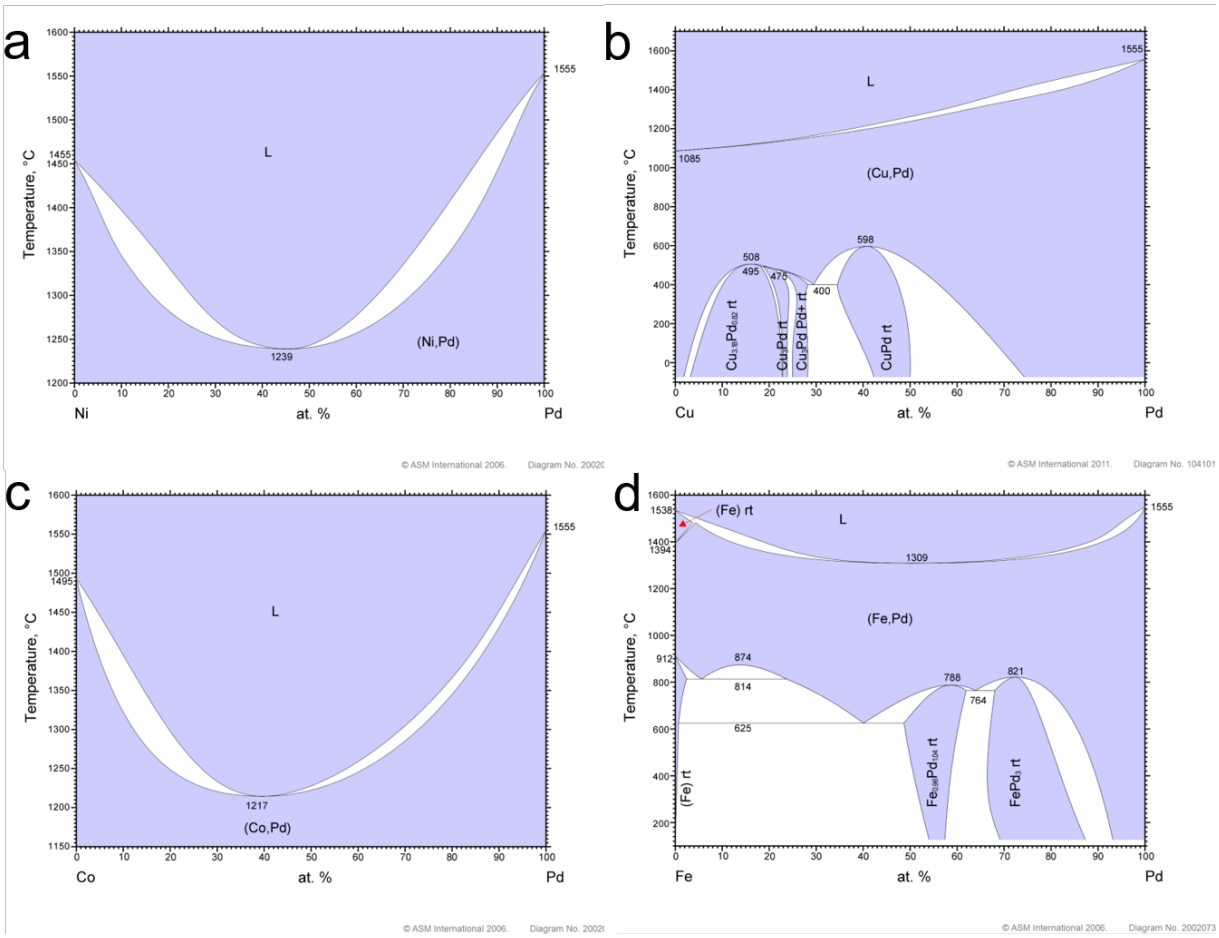

Figure 3.16 *Phase diagrams of (a)Pd-Ni[80], (b) Pd-Cu[81], (c) Pd-Co[80] and (d)Pd-Fe.*[82]

This is possibly due to the formation of metastable binary alloys over those multi-phase regions during the ultrafast cooling process from gas-phase sputtered atoms into solid-phase metal films. The formation of Pd-Co fcc-type solid solutions are mostly successful except the very Co-rich alloys (Pd_5Co_{95}, which is a single-phase hcp-type alloy with similar crystal symmetry as the fcc-type alloys. It is noticeable in the miscible phase diagram of Pd-Co (Figure 3.16(c)). In Pd-Fe alloys, up to around 50% can be incorporated into the Pd lattice to form fcc-type Pd-Fe alloys. However, further increase in Fe at.% to 69% or higher would induce the formation of bcc-type Pd-Fe alloys with a much smaller lattice parameter. Those observation in XRD is consistent with the phase distribution in the Pd-Fe phase diagram (Figure 3.16(d)). When Fe at.% is larger than 50%,

thermodynamically, Fe prefers not to form a solid solution with Pd. The reason for forming bcc-type Pd-Fe alloys is that the sputtering process bombards Pd ions into the bcc-type lattice of Fe to form the metastable alloys. Pd-Mn thin films have large mismatch. The difference in lattice parameters of Pd and Mn is as large as 21%, which would not allow for the formation of single-phase solid solutions, even no metastable compositions under current sputtering conditions.

3.3 RDE

After the structures and compositions are thoroughly examined by XRD and SEM-EDX, Pd-M thin films are tested as the electrocatalysts for the ORR in alkaline fuel cells. Pd-M/Ti/GC electrodes are loaded into the replaceable disk setup for RDE measurements in 1M KOH at a scan rate of 5 mV/s and rotation rate of 1600 rpm. RDE measurements in 1M KOH, relative to 0.1M KOH, is closer to the realistic OH^- concentration (2~3 M) in practical membrane electrode assembly (MEA) tests. [83] Based on the Levich equation, the i_d of the $4e^-$ reduction of oxygen in 0.1 M oxygen saturated KOH or $HClO_4$ should be around -5.5 mA/cm^2 at 1600 rpm. Since the O_2 solubility in 1M KOH at 25 ^oC and 1 atm is 8.42×10^{-4} mol/L, which is 70% of C_{O_2} in 0.1 M KOH (1.21×10^{-3} mol/L), [84] the i_d of the 4e- ORR in 1M KOH will be correspondingly lower with a value of -3.7 mA/cm^2 at 1600rpm.

3.3.1 Pd-Cu

As shown in Figure 3.17, Pd-Cu thin films are able to achieve the I_d of around -3.7 mA/cm^2, suggesting a $4e^-$ process of reducing O_2 completely to H_2O. Pd-Cu thin films with Pd at.% from 32% to 7% exhibit an I_d less than -3.5 mA/cm^2, indicating a larger contribution of peroxide formation during the $2e^-$ process. Lowering the Pd at.% from 32% to 7% also causes a noticeable drop in the half-wave potential ($E_{1/2}$). To quantitatively assess the activity of various Pd-M thin

films, the kinetic current (i_k) at 0.9 V is calculated, based on the Koutecky-Levich equation ($1/i = 1/i_d + 1/i_k$ where i and i_d are the measured current, diffusion-limited current).

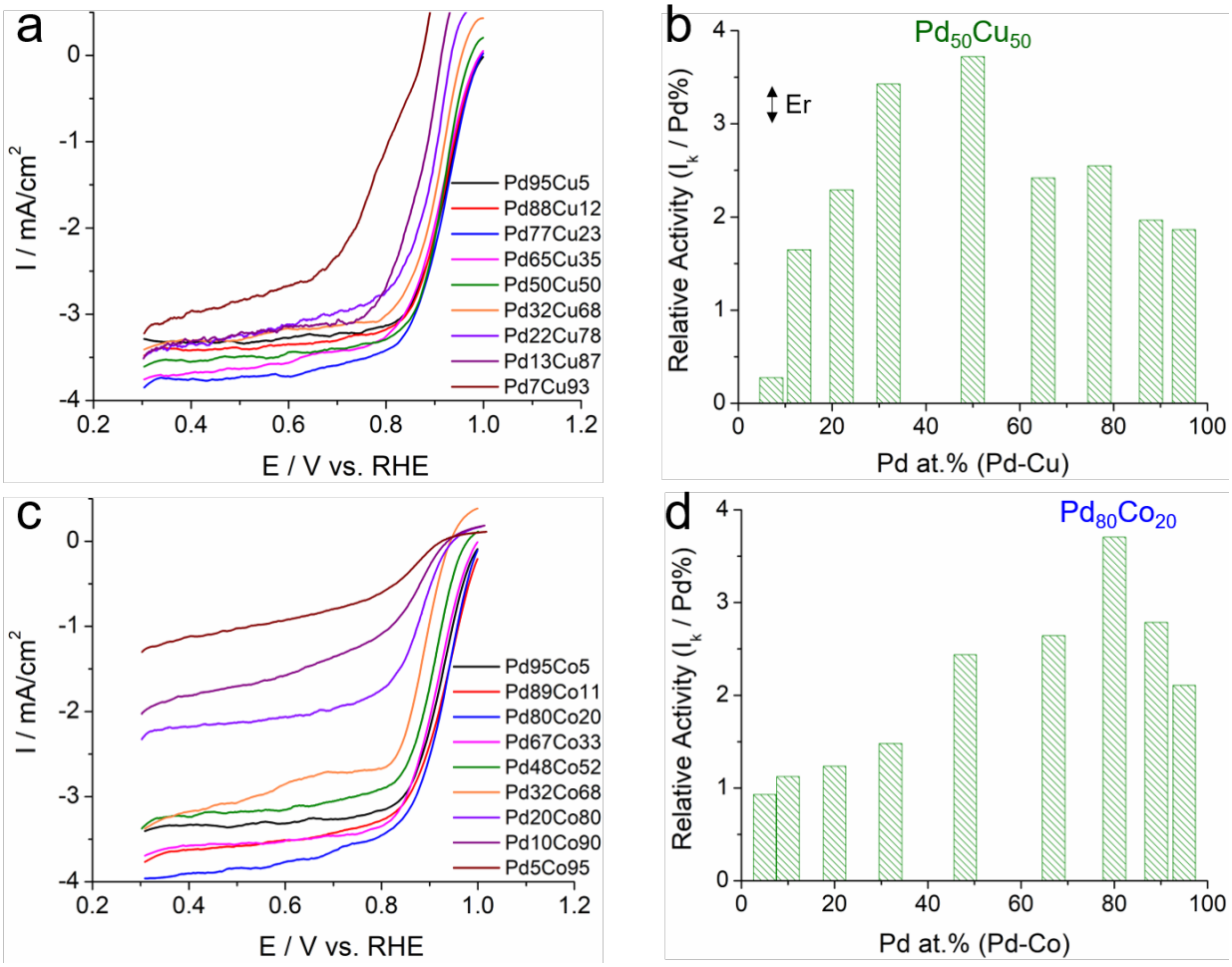

Figure 3.17 *(a) ORR polarization profiles of Pd-Cu thin films at 5 mV/s and 1600 rpm, and (b) the corresponding the relative activity (i_K@ 0.9 V vs. Pd at.%), with an optimal value at $Pd_{50}Cu_{50}$ (c) ORR polarization profiles of Pd-Co thin films at 5 mV/s and 1600 rpm, and (d) the corresponding the relative activity (i_K @ 0.9 V vs. Pd at.%), with an optimal value at $Pd_{80}Co_{20}$*

The relative Pd at.% can represent the relative coverage of Pd on the surface. Normalizing the i_K to Pd at.% provides a high-throughput method to calculate the intrinsic activity per Pd site, which is named as the "relative activity". As shown in Figure 3.17 (b), the relative activity of various Pd-Cu thin films follows a volcano plot with the optimal activity at $Pd_{50}Cu_{50}$. The relative activity of $Pd_{50}Cu_{50}$ is about two times as high as that of the nearly pure Pd film ($Pd_{95}Cu_5$). Further

increase of the Cu at.% above 50% causes a gradual decrease of the relative activity and eventually a significantly low activity at Pd_7Cu_{93} (only 15% of the relative activity of $Pd_{95}Cu_5$).

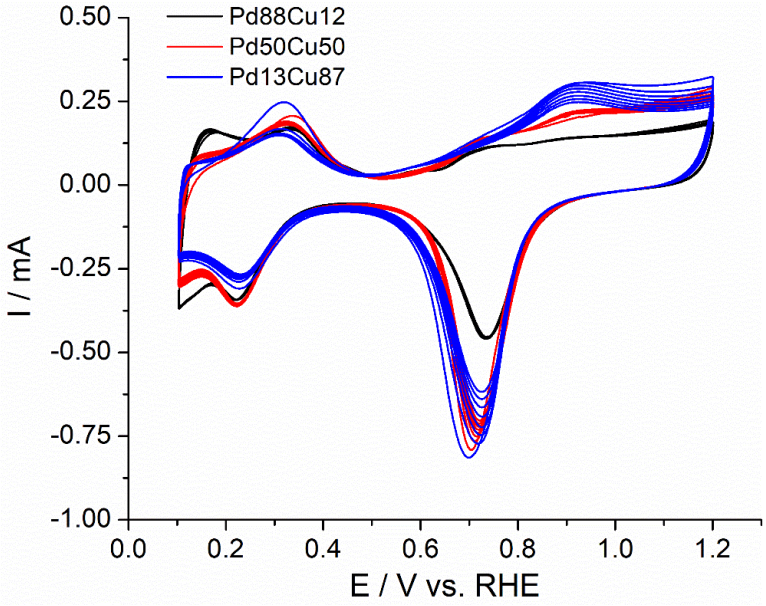

Figure 3.18 *CV profiles of three kinds of Pd-Cu films at 20mV/s in Ar-sat. 1M KOH.*

CV profiles of Pd-Cu thin films shows that when lowering Pd contents from $Pd_{88}Cu_{12}$ to $Pd_{50}Cu_{50}$ and $Pd_{13}Cu_{87}$, the hydrogen region (0.1-0.2 V) is suppressed as a result of less Pd sites on the surface (Figure 3.18). Less Pd contents also causes larger reduction peaks near 0.7 V, which is due to the formation of larger amount of Cu oxide during the previous positive scan. Basically, those RDE results indicate the $Pd_{50}Cu_{50}$ could serve as a promising composition as an ORR catalyst for alkaline fuel cell.

3.3.2 Pd-Co

RDE measurements of Pd-Co are performed under same test conditions in 1M KOH. As shown in Figure 3.17, reducing Pd at.% from 95% to 67% did not result in a significant change in the early kinetic-controlled region (0.9-1.0 V). Further lowering the Pd at.% from 48% to 5% causes a dramatic decrease in both the half-wave potential as well as the i_d, suggesting Pd at.%

(<50%) would induce a larger contribution from the $2e^-$ peroxide formation, especially for Pd at.% less than 20%. The relative activity increases from $Pd_{95}Co_5$ to $Pd_{80}Co_{20}$ and then continuously decreases from $Pd_{80}Co_{20}$ to Pd_5Co_{95} (Figure 3.17 (d)).

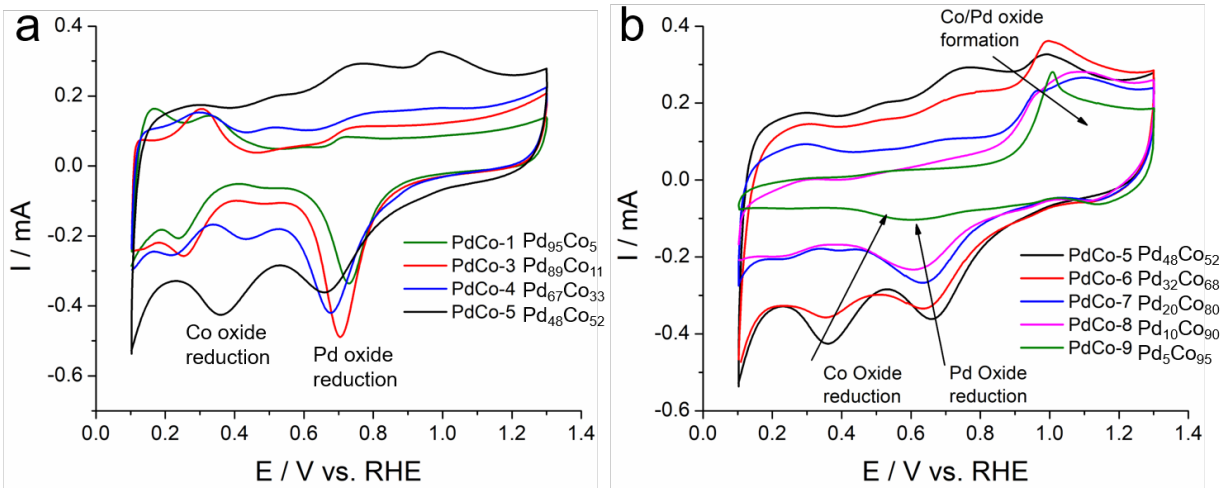

Figure 3.19 *CV profiles of (a) Pd-rich Pd-Co films and (b) Co-rich Pd-Co films at 20mV/s in Ar-sat. 1M KOH.*

CV profiles of Pd-Co thin films show the involvement of the co-existence of two redox couples (Pd/Pd oxides and Co/Co oxides, Figure 3.19). $Pd_{95}Co_5$ and $Pd_{89}Co_{11}$ show the characteristic hydrogen regions of Pd with the peak near 0.2V corresponding to the underpotential deposition of hydrogen atoms (H_{UPD}) (Figure 3.19 (a)). Further increase in Co at.% to $Pd_{67}Co_{33}$ and $Pd_{48}Co_{52}$ shows the noticeable reduction peak at around 0.4 V, which correspond to the reduction of Co oxide and suggest Pd and Co co-existed on the surface of thin films. In the Co-rich films, the reduction peak of Pd oxide gradually decreases from $Pd_{48}Co_{52}$ to $Pd_{10}Co_{90}$ with less pronounced hydrogen regions (Figure 3.19 (b)). Very Co-rich Pd_5Co_{95} film almost only shows the redox couple of Co (1.1V/0.6V) given the little amount of Pd. Therefore, those results indicate $Pd_{80}Co_{20}$ (i.e., Pd_4Co) could be a potential composition for the catalyst.

3.3.3 Pd-Fe and Pd-Ni

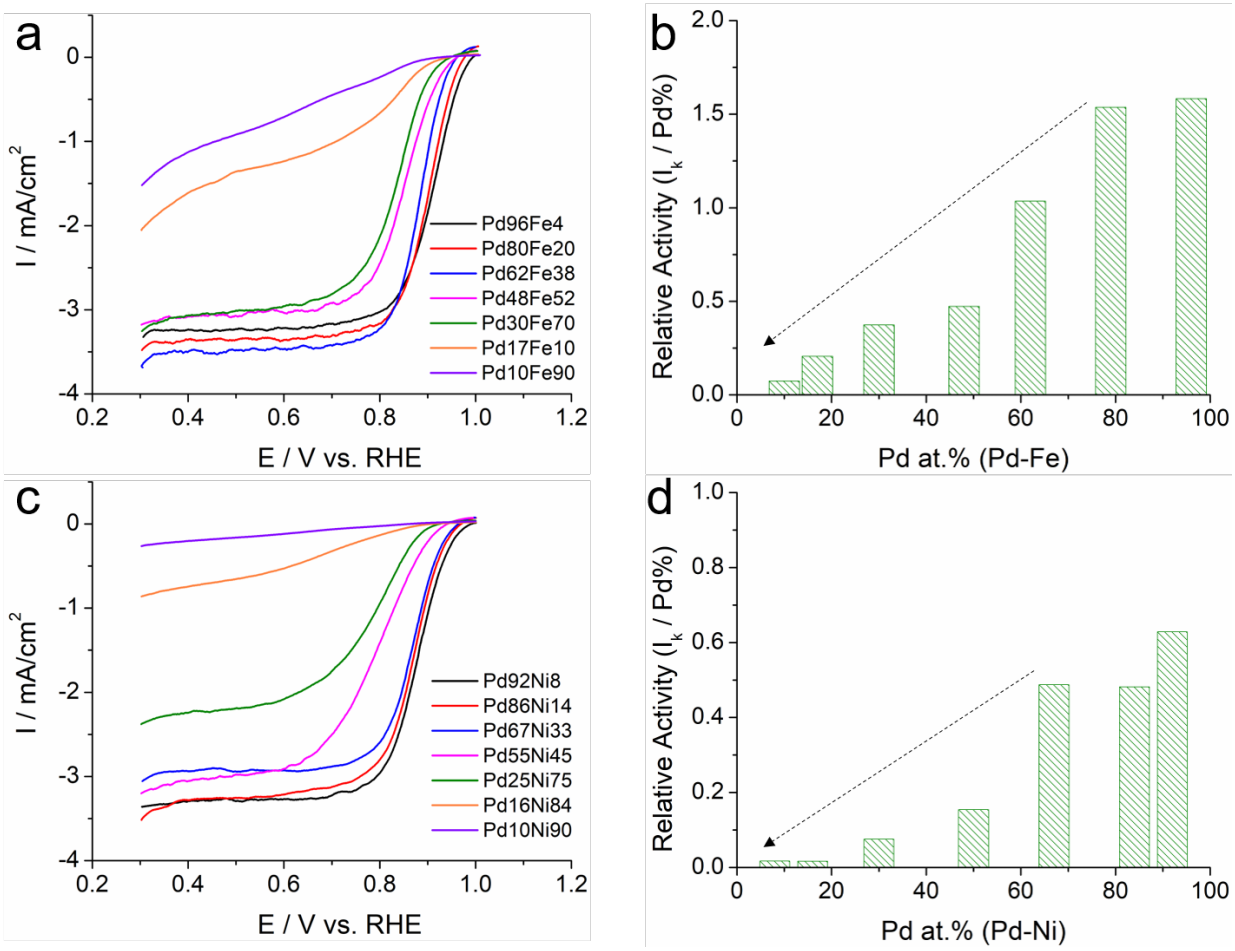

Figure 3.20 *(a) ORR polarization profiles of Pd-Fe thin film at 5 mV/s and 1600 rpm in O2-sat. 1M KOH, and (b) the corresponding the relative activity (i_K @ 0.9 V vs. Pd at.%), with a monotonic activity decay at less Pd at.% (c) ORR polarization profiles of Pd-Ni thin films at 5 mV/s and 1600 rpm, and (d) the corresponding the relative activity (i_K @ 0.9 V vs. Pd at.%) of Pd-Ni, with the similar trend as Pd-Fe system.*

As shown on Figure 3.20, ORR activities of Pd-Fe and Pd-Ni are also measured under same test conditions in 1M KOH. When Pd at.% decreases from $Pd_{96}Fe_4$ to $Pd_{30}Fe_{70}$, Pd-Fe thin films exhibit a near-4e$^-$ process with a gradual decay in the $E_{1/2}$. Further decrease of Pd at.% from $Pd_{30}Fe_{70}$ to $Pd_{10}Fe_{90}$ causes a significant loss in the i_d, indicating a larger contribution from 2e$^-$ peroxide formation. The calculated relative activity of Pd-Fe thin film shows an monotonic decay as Pd at.% decreases from 96% to 10% (Figure 3.20 (b)). When the Pd at.% in Pd-Ni film decreases

from $Pd_{92}Ni_8$ to $Pd_{10}Ni_{90}$, Pd-Ni thin film shows a similar trend in the ORR polarization profiles (Figure 3.20 (c)) and calculated relative activity (Figure 3.20 (d)). CV profiles of Pd-Fe and Pd-Ni films suggest a gradual loss of H_{UPD} regions from $Pd_{96}Fe_4$ to $Pd_{17}Fe_{83}$ and from $Pd_{86}Ni_{14}$ to $Pd_{16}Ni_{84}$ (Figure 3.21).

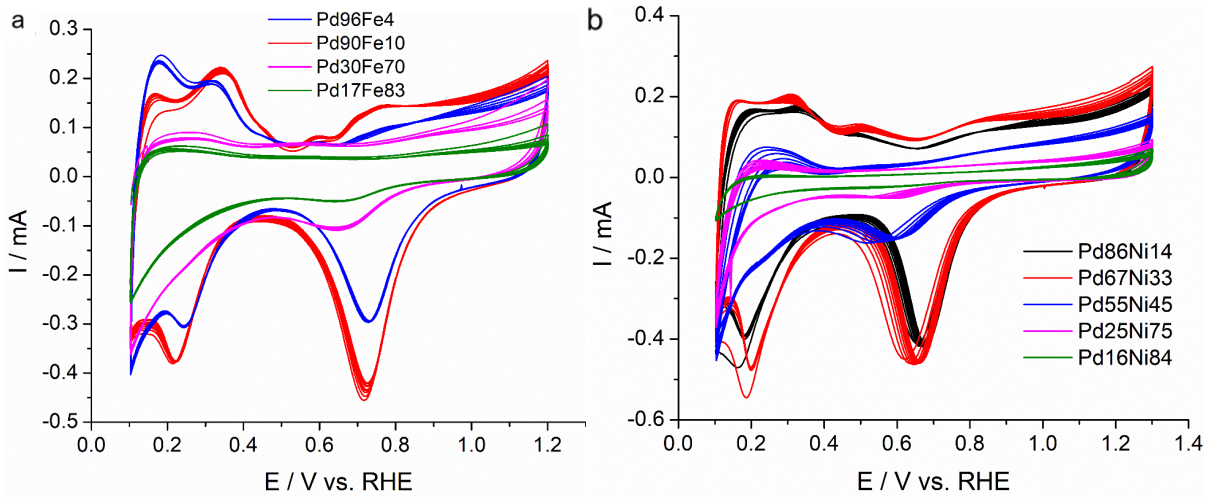

Figure 3.21 *(a) CV profiles of four kinds of Pd-Fe films at 20mV/s in Ar-sat. 1M KOH. (b) CV profiles of five kinds of Pd-Ni films at 20mV/s in Ar-sat. 1M KOH.*

3.4 Conclusion

As a conclusion, ORR activities of four families of Pd-Cu, Co, Fe and Ni binary alloys are examined using replaceable disk electrodes in RDE measurements. $Pd_{50}Cu_{50}$ and $Pd_{80}Co_{20}$ show optimal activities among Pd-Cu and Pd-Co thin film electrodes. Figure 3.17 (b) and Figure 3.17 (d) show volcano graphs about the relative activity. On the other hand, Pd-Fe and Pd-Ni show a monotonic activity decay as a result of the decrease of Pd at.%. The composition of $Pd_{50}Cu_{50}$ is the best among all those materials. And this will provide a guide line to a parallel nanoparticle synthesis research operated by Y.Yang and Abruña Group.

4. Divergence, Challenges, and Future Outlook

The short two-year journey at Cornell is about to end. This is a journey about learning and growing. Along the way, there are a series of unsuccessful experiments, unsolvable challenge and attempts to challenge the "doesn't work" projects. Those are failure, puzzles, pity, and things can't be done due to the limitation of time. I will conclude them here with the future outlook of this project.

4.1 Divergence

4.1.1 Pd-Mn, Pd-V and Pd-Cr

It might be noticed that Pd-Mn has been poorly covered in this thesis. That's because of the unsuccessful mix of the solid solution. Even under sputtering conditions, the metastable solid solution is still hardly formed. The same problem happens on Pd-V (Figure 4.1) and Pd-Cr (Figure 4.2). Here, both Figures show the pattern on Pd rich positions shows Pd (111) peak dominant where no peak sliding happens like Pd-Cu, Co, Fe, and Ni. On the poor Pd side, the patterns only show the V (110) and Cr (110) peaks as well. For both materials, those are not miscellaneous reactions. According to the phase diagram (Figure 4.3), Cr and V are hardly mixable with Pd like Mn. Again, it is unable to form metastable phases even under sputtering. It is not a good idea to challenge thermodynamics.

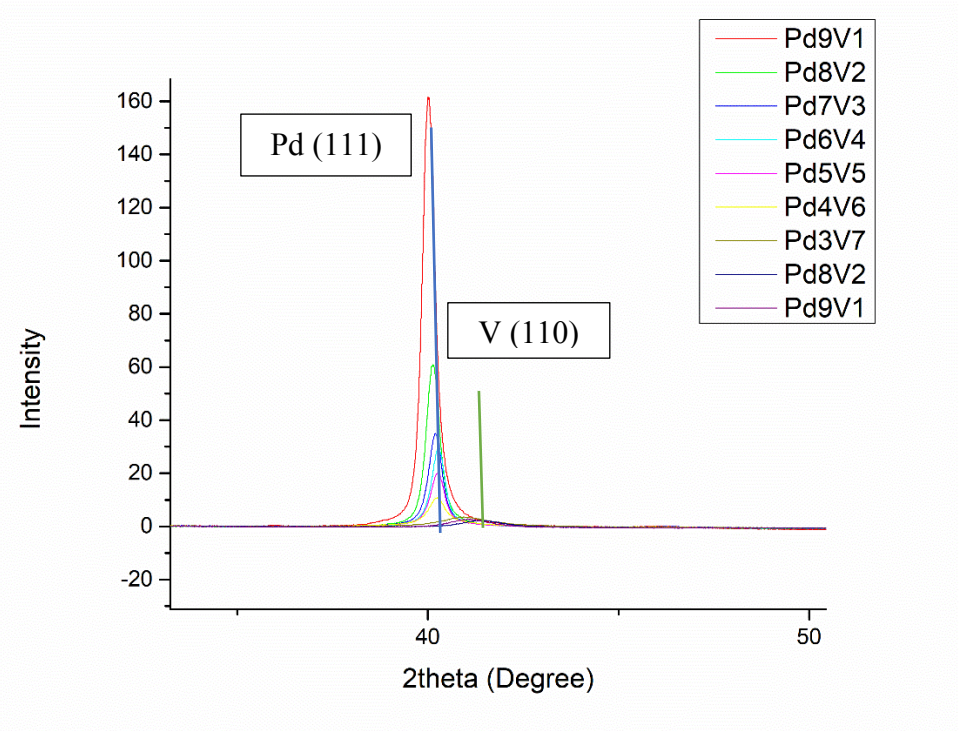

Figure 4.1 *Pd-V XRD pattern*

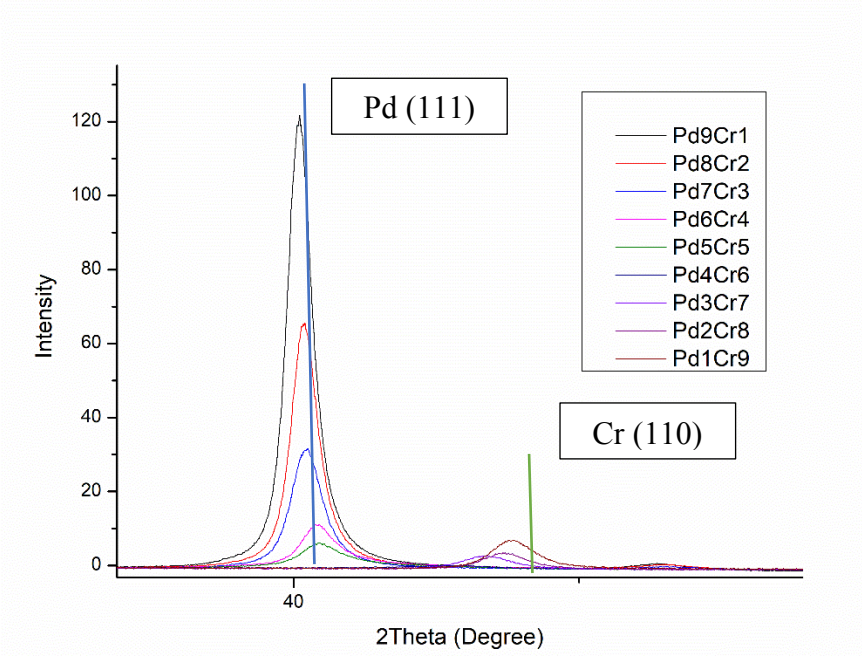

Figure 4.2 *Pd-Cr XRD pattern*

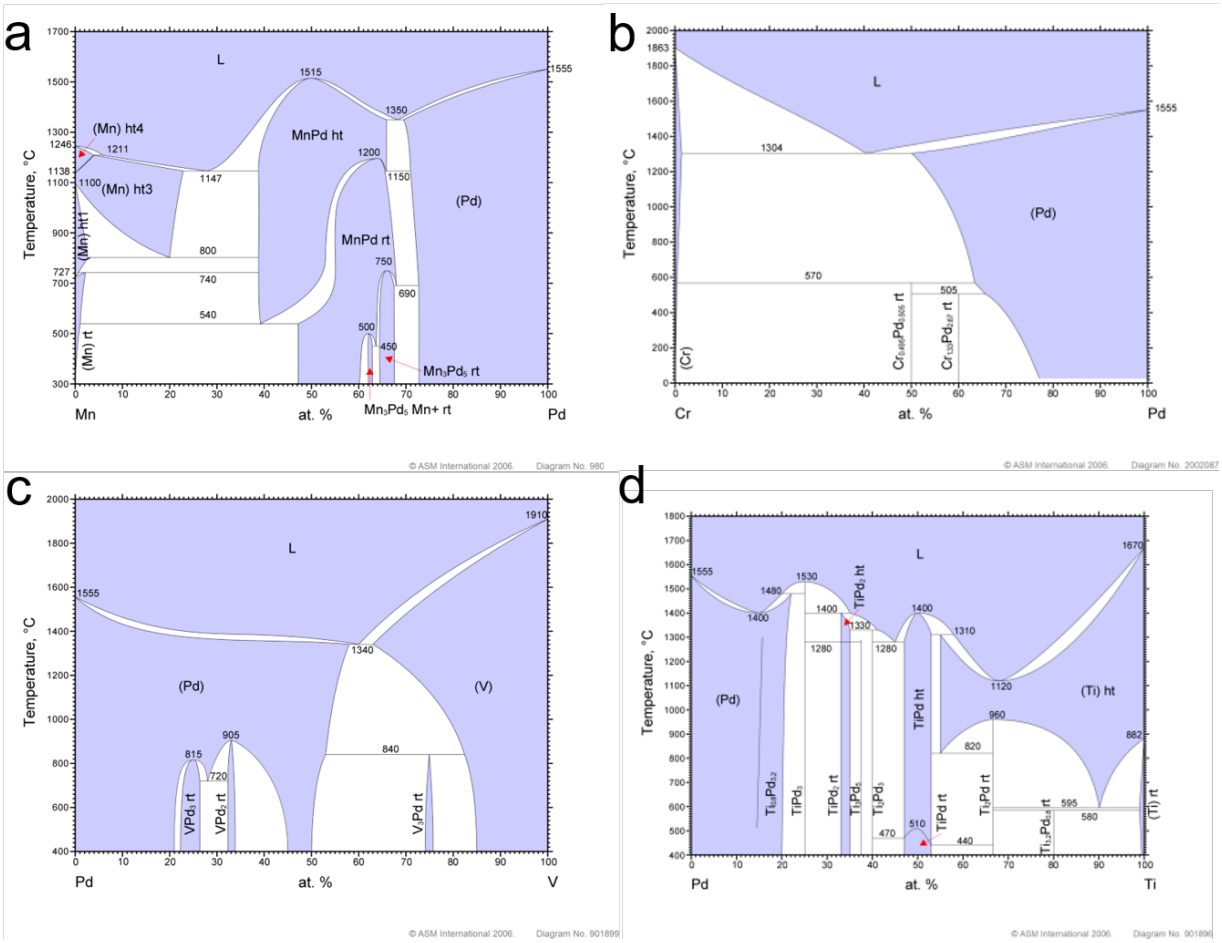

Figure 4.3 *Phase diagrams of (a)Pd-Mn[85], (b)Pd-Cr[86], (c)Pd-V[87] and (d)Pd-Ti[88].*

4.1.2 Mn-Co Oxide

Mn_2CoO_4 shows promising catalytic activity as ORR catalyst due to the existence of the spinel structure. [8990] The raw materials (Mn, Co) are much cheaper than Pt. This could be a direction brings revolution to the fuel cell industry. In the previous work in nanoparticle synthesis, $Mn_{1.5}Co_{1.5}O_4$ shows promising activity among all the compositions. However, as mentioned previously, nanoparticle synthesis is rather a slow process with hurdle controlling the composition, crystal structure etc. On the other hand, thin film has been an untouched field for this topic and magnetron sputtering is efficient in preparing gradient composition samples with reactive sputtering. Therefore, Mn-Co Oxide becomes the first materials we study.

At the beginning of the study, we faced adhesive problem where films peeled off from GC substrate during RDE. Adding Ti adhesive layer solved the problem. The graph below shows the cross-section mapping of SEM-EDS. The Ti layer lies clearly between the film and the substrates. However, the Ti layer also introduced a decay in catalytic activity (Figure 4.5), and this makes the activity of the thin film materials lag far behind the nanoparticles, not to mention Pt/C.

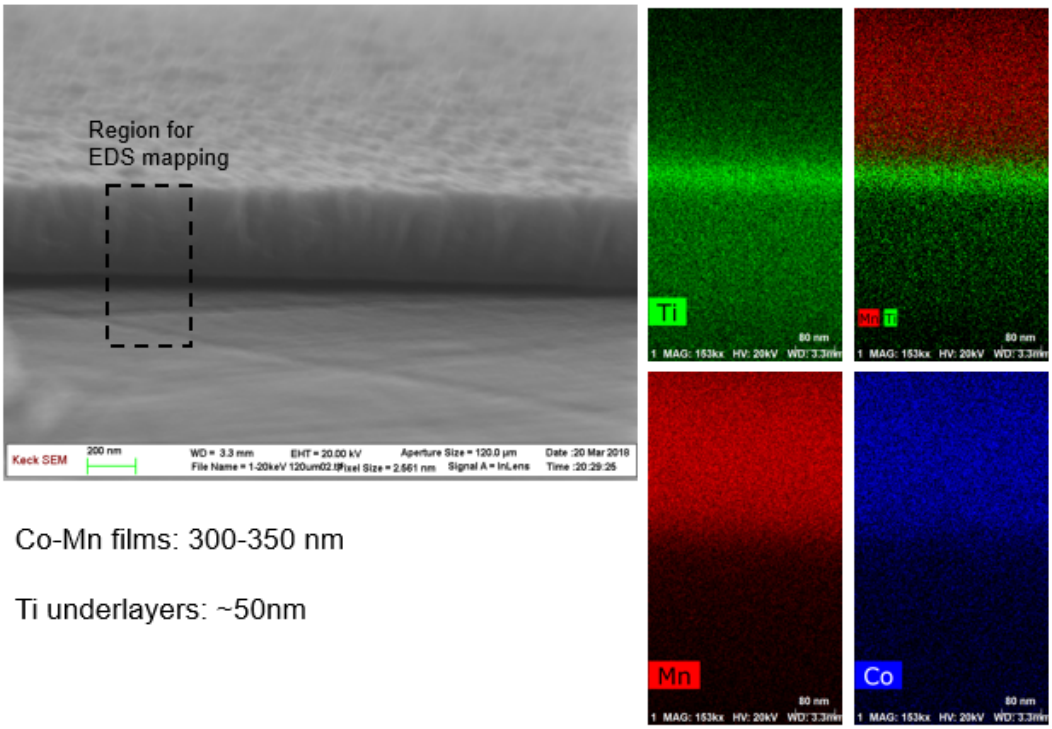

Figure 4.4 *Cross Sectional SEM-EDS mapping for Mn4CoO4/Ti/GC electrode. The boarders between Mn-Co Oxide, Ti underlayer and GC substrates are clear.*

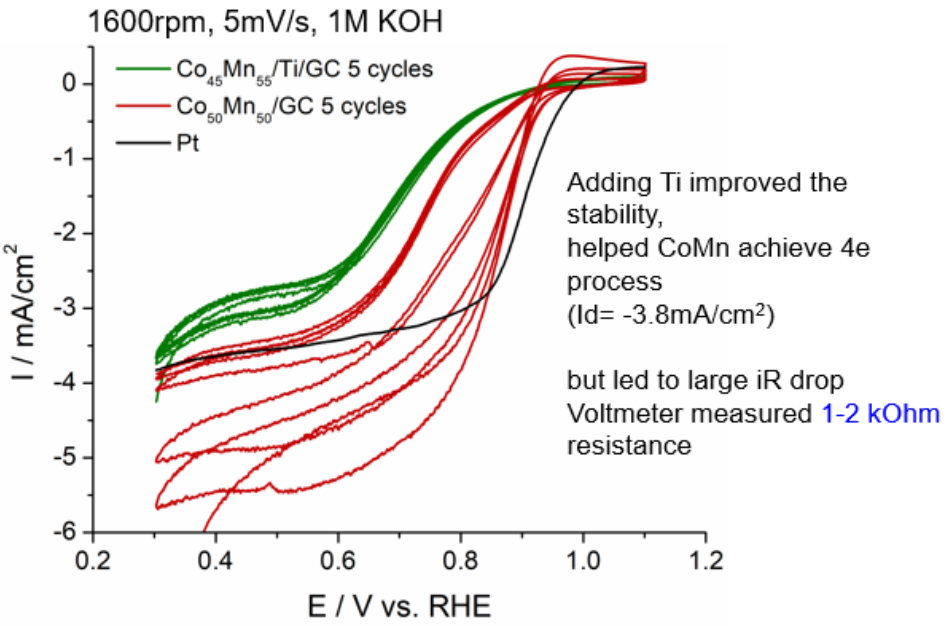

Figure 4.5 *RDE result of Mn-Co oxide, Mn-Co oxide with Ti underlayer, and Pt as reference*

The hypothesis of this phenomenon is the formation of TiO_2 that increase the overall resistivity of the sample and hindering electron transfer during RDE. Several different approaches are trailed to minimize the effect caused by TiO_2 including thinner Ti layer (Figure 4.6), and replacing Ti with Nb (Figure 4.7). Even though the $E_{1/2}$ increases with thinner Ti films, the gap between the best thin film and the nanoparticle is still huge (0.65V vs 0.85V) (Figure 4.8). Afterall none of these methods became decent solution to the iR drop.

Therefore, the reason for the drop stays mystery for now. There might be some interaction between Mn and Ti; when I later directly deposited Mn-Co on top of 50nm Ti underlayer on top of silicon wafer, the Mn part of the film peeled off. However, due to time limit, we switch to Pd for the screen methodology.

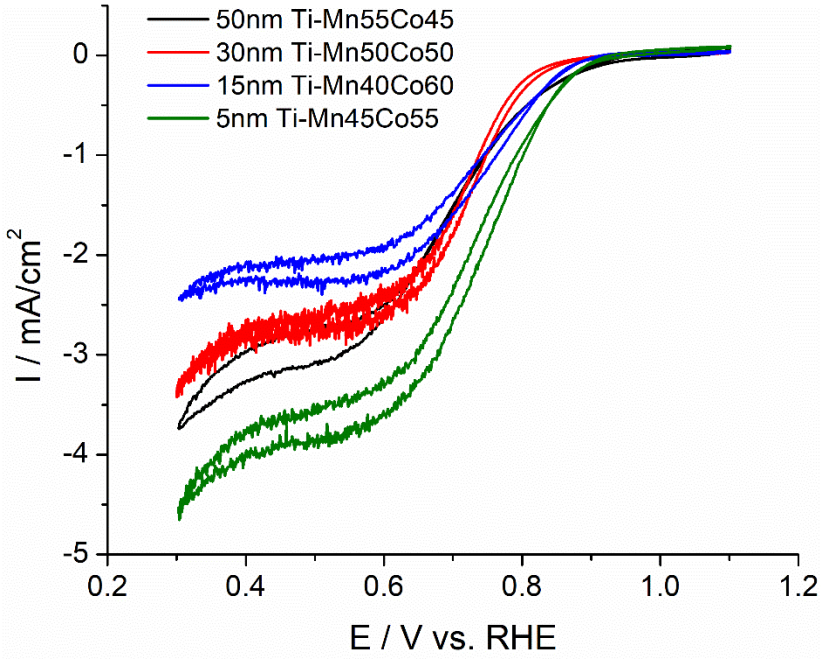

Figure 4.6 *RDE results for Mn-Co oxide with different thickness of Ti underlayer*

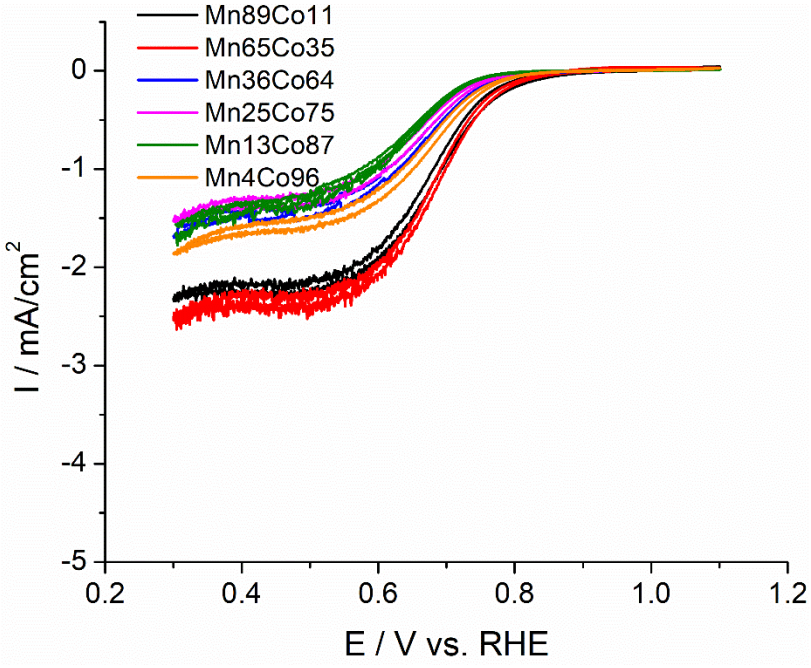

Figure 4.7 *RDE results of Mn-Co Oxide with Nb underlayer*

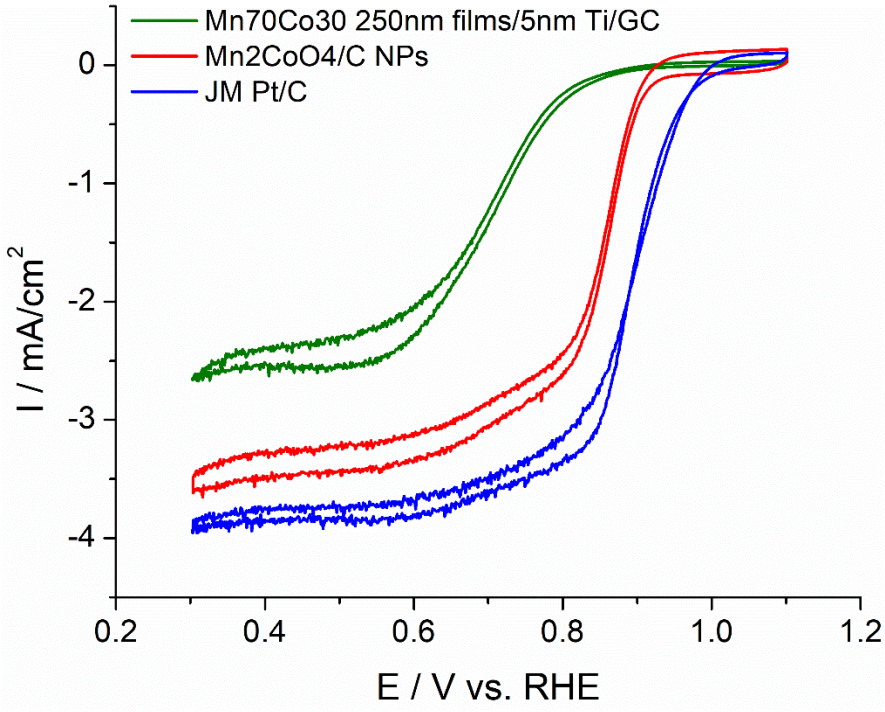

Figure 4.8 *RDE results of optimal thin film Mn-Co oxide, nanoparticle Mn2CoO4, and reference Pt/C*

4.2 Challenge

4.2.1 Adhesive problem

As mentioned above, the adhesion of film on GC substrate became a problem during both Mn-Co Oxide research and Pd-M research. In the case of Pd-M, adding a 50nm Ti underlayer solved most of the stability problem except Pd-V which still peeled off in the V rich side. The guess for the reason is the build up of internal pressure on the film and no alloy was formed in the part of the film as well. This can be proved by XRD result (Figure 4.1) and the phase diagram (Figure 4.3 (c)).

For Mn-Co oxide, the adhesive Ti layer became a big hurdle during electrochemical characterization which introduced a huge iR drop. If this problem can be solved, the direction of Mn-Co oxide would be worth to further dig into.

4.2.2 SEM-EDS vs XPS

There is a contradiction between SEM-EDS and XPS result on Pd-Cu samples. In EDS, the 50% Pd composition appears in position 5 (Figure 3.1 (b)). However, in XPS, the position 5 shows (Figure 4.9). This could be critical since this is the optimal activity position and the Pd composition is off by 50%. At the same time, the electrochemical characterization process is surface sensitive which is identical with XPS; if we put that in this way, the XPS result is more reliable. But on the other hand, it is hard to explain why position 5 will have more Pd since the surface tension of Cu is less than that of Pd (0.69 eV vs 0.77 eV)[91]. Through the calibration, the deposition rate of Cu and Pd are both set to be 2.5 Å/s at the center of two sputter guns. The composition is the same in bulk which proved by the EDS result but the reason why the surface is different stays a myth.

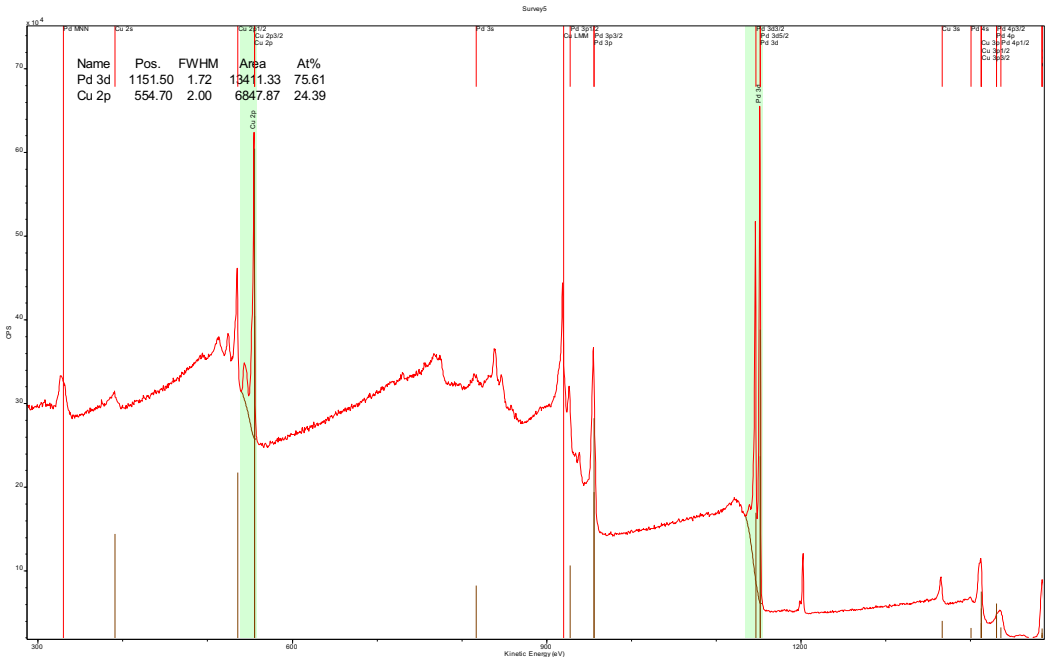

Figure 4.9 ***XPS result at position 5 of the Pd-Cu shows 75 at. % of Pd***

4.3 Future Outlook

4.3.1 Fuel Cell

The commercialization development of fuel cell pauses for now and waits for a new cheap, efficient catalytic material to bring revolution to the industry. There are many different options in the lab, yet Pt/C is still the most approachable material for fuel cells. The research about Pd is our yield to both time limit and unsolvable challenge. The price of Pd ($1.5K per Ounce) [92] is almost twice as expensive as Pt ($813.65 per Ounce)[93]. Even though the Pd price fluctuate throughout history, the price experience almost exponentially growth since 2008. [94] Therefore, the commercial value of the Pd catalysts remains a question.

For fuel cell itself, there is no doubt that hydrogen power, and fuel cell technology, are the most realized future clean energy source. However, there are still some problems remains: cost,

storage, water splitting etc. It is exciting to discover that new technologies related to this field are keeping popping out, e.g. photocatalytic water splitting solar cells [95].

In the scope of this project, Yao Yang will operate a parallel nanoparticle synthesis project following the optimal material Pd_{50} Cu_{50} screened by this study. I wish what Yao and I have done here at Cornell can help the researchers in this area and give them illumination if possible.

4.3.2 Sputtering

Sputtering is a mature PVD methods which has been thoroughly studied by the researcher around 30 years ago. On the other hand, 3D printing is a newly developed technology with many problems waiting for solutions, e.g. expensive and high energy laser required metal printing methods (Power bed fusion, Direct Energy Deposition etc.)[96] Combining 3D printing and plasma sputtering might be an interesting direction to investigate. Parameswaran et al at MIT Lincoln Laboratory are utilizing atmospheric plasma sputtering on 3D printing to make metal printing easier[97]. However, the drawback for sputtering is obvious compare to those high energy options, which is the lower deposition rate.

Old technology can always combine and integrate with something new; sputtering still has great potential in both academic and application.

REFERENCES

1 Ingram, A. (2014, April 14). Toyota Gasoline Engine Achieves Thermal Efficiency Of 38 Percent. Retrieved from https://www.greencarreports.com/news/1091436_toyota-gasoline-engine-achieves-thermal-efficiency-of-38-percent

2 CO2 Emissions from Fuel Combustion – Highlights, International Energy Agency (2017), http://www.iea.org/publications/freepublications/publication/CO2EmissionsFromFuelCombustionHighlights2017.pdf

3 New York State Energy Profile. (n.d.). Retrieved from https://www.eia.gov/state/print.php?sid=NY

4 The Social Cost of Carbon. (2017, January 09). Retrieved from https://19january2017snapshot.epa.gov/climatechange/social-cost-carbon_.html

5 Groger, O., Gasteiger, H., & Suchslandc, J. (2015). Review—Electromobility: Batteries or Fuel Cells? Journal of The Electrochemical Society,162, 14th ser., A2605-A2622. Retrieved June 18, 2019.

6 The Longest-Range Electric Vehicle Now Goes Even Farther. (2019, May 10). Retrieved from https://www.tesla.com/blog/longest-range-electric-vehicle-now-goes-even-farther

7 Debe, M. K. Electrocatalyst Approaches and Challenges for Automotive Fuel Cells. Nature. 2012, 486, 43-51.

8 Gasteiger, H. A.; Kocha, S. S.; Somali, B.; Wagner, F. T. Activity Benchmarks and Requirements for Pt, Pt-alloy, and non-Pt Oxygen Reduction Catalysts for PEMFCs. Appl. Catal., B. 2005, 56, 9-35.

9 Lipman, T. E. (2019). Fuel cells and hydrogen production: A volume in the Encyclopedia of sustainability science and technology, Second edition. New York, NY: Springer.

10 Antolini, E. (2009). Palladium in fuel cell catalysis. Energy & Environmental Science,2(9), 915. doi:10.1039/b820837a

11 Ayers, K.; Dalton, L.; Roemer, A.; Carter, B.; Niedzwiecki, M.; Manco, J.; Anderson, E.; Capuano, C.; Wang, C.-Y.; Zhao, W.(2014) High Performance, Low Cost Hydrogen Generation from Renewable Energy. U.S. Department of Energy Technical Report., DOI: 10.2172/1117668.

12 Papageorgopoulos, D. (2017) Annual Merit Review and Peer Evaluation Meeting in Fuel Cells Program Area. U.S. Department of Energy, Washington, DC, June 5-9,.

13 Wang, D.; Xin, H. L.; Hovden, R.; Wang, H.; Yu, Y.; Muller, D. A.; DiSalvo, F. J.; Abruña, H. D. (2012) Structurally Ordered Intermetallic Platinum-Cobalt Core-Shell Nanoparticles with Enhanced Activity and Stability as Oxygen Reduction Electrocatalysts. Nat. Mater, 12, 81-87.

14 Xiong, Y.; Yang, Y.; DiSalvo, F. J.; Abruña, H. D. (2018) Pt-Decorated Composition-Tunable Pd–Fe@Pd/C Core–Shell Nanoparticles with Enhanced Electrocatalytic Activity toward the Oxygen Reduction Reaction J. Am. Chem. Soc, 140, 7248-7255.

15 Lima, F.; Zhang, J.; Shao, M.; Sasaki, K.; Vukmirovic, M.; Ticianelli, E.; Adzic, R. (2007) Catalytic Activity−d-Band Center Correlation for the O2 Reduction Reaction on Platinum in Alkaline Solutions. J. Phys. Chem. C, 111, 404-410.

16 Yang, Y.; Xiao, W.; Feng, X.; Xiong, Y.; Gong, M.; Shen, T.; Lu, Y.; Abruña, H. D.; Wang, D. Golden Palladium Zinc Ordered Intermetallics as Oxygen Reduction Electrocatalysts. ACS Nano 2019, 13, 5968-5974.

17 Jiang, G.; Zhu, H.; Zhang, X.; Shen, B.; Wu, L.; Zhang, S.; Lu, G.; Wu, Z.; Sun, S., (2015) Core/Shell Face-Centered Tetragonal FePd/Pd Nanoparticles as an Efficient Non-Pt Catalyst for the Oxygen Reduction Reaction. ACS nano, 9, 11014-11022.

18 Wang, D.; Xin, H. L.; Wang, H.; Yu, Y.; Rus, E.; Muller, D. A.; DiSalvo, F. J.; Abruña, H. D., Facile synthesis of carbon-supported Pd–Co core–shell nanoparticles as oxygen reduction electrocatalysts and their enhanced activity and stability with monolayer Pt decoration. Chem. Mater. 2012, 24, 2274-2281.

19 Xiao, W.; Cordeiro, M. A. L.; Gong, M.; Han, L.; Wang, J.; Bian, C.; Zhu, J.; Xin, H. L.; Wang, D. (2017) Optimizing the ORR activity of Pd based nanocatalysts by tuning their strain and particle size. J. Mater. Chem. A, ,5, 9867-9872

20 Luo, L.; Zhu, F.; Tian, R.; Li, L.; Shen, S.; Yan, X.; Zhang, J. (2017) Composition-Graded PdxNi1−x Nanospheres with Pt Monolayer Shells as High-Performance Electrocatalysts for Oxygen Reduction Reaction. ACS Catal., 7, 5420-5430.

21 Shao, M.; Shoemaker, K.; Peles, A.; Kaneko, K.; Protsailo, L (2010). Pt Monolayer on Porous Pd-Cu Alloys as Oxygen Reduction Electrocatalysts. J. Am. Chem. Soc., 132-9253-9255.

22 Haile, S. (2003). Fuel cell materials and components. Science Direct,51, 5981-6000.

23 Schumm, B. (2018, December 20). Fuel cell. Retrieved from https://www.britannica.com/technology/fuel-cell

24 Wei, C., Rao, R. R., Peng, J., Huang, B., Stephens, I. E., Risch, M., . . . Shao-Horn, Y. (2019). Recommended Practices and Benchmark Activity for Hydrogen and Oxygen Electrocatalysis in Water Splitting and Fuel Cells. Advanced Materials,1806296. doi:10.1002/adma.201806296

25 E. Gülzow, M. Schulze, (2004), Long-term operation of AFC electrodes with CO2 containing gases, Journal of Power Sources 127, 243–251.

26 G.F. McLean, T. Niet, S. Prince-Richard, N. Djilali, (2002) An assessment of alkaline fuel cell technology, International Journal of Hydrogen Energy 27, 507–526.

27 J. Larminie, A. Dicks, (2002) Fuel cell Systems Explained, J. Wiley, , pp. 109–122.

28 Merle, G., Wessling, M., & Nijmeijer, K. (2011). Anion exchange membranes for alkaline fuel cells: A review.Journal of Membrane Science,1-35. doi:10.1002/9781118869345.ch05

29 E. Agel, J. Bouet, J.F. Fauvarque, (2001) Characterization and use of anionic membranes for alkaline fuel cells, Journal of Power Sources 101, 267–274.

30 L. Akrour,(2005) Membrane échangeuse anionique et application en pile à combustible, CNAM, Paris, France,.

31 T. Xu, Z. Liu, W. Yang, (2005) Fundamental studies of a new series of anion exchange membranes: membrane prepared from poly(2,6-dimethyl-1,4-phenylene oxide) (PPO) and triethylamine, Journal of Membrane Science 249, 183–191

32 Jacob S. Spendelow and Andrzej Wieckowski. (2007) Electrocatalysis of oxygen reductionand small alcohol oxidation in alkaline media. Physical Chemistry Chemical Physics,9(21):26-54.

33 Ge, X., Sumboja, A., Wuu, D., An, T., Li, B., Goh, F. W., . . . Liu, Z. (2015). Oxygen Reduction in Alkaline Media: From Mechanisms to Recent Advances of Catalysts. ACS Catalysis,5(8), 4643-4667. doi:10.1021/acscatal.5b00524

34 M. R. Tarasevich, A. Sadkowski, and E. Yeager, Comprehensive Treatise of Electrochemistry, vol. 7 (B. E. Conway, ed.) (Plenum, New York, 1983), Ch. 6.

35 Shao, M. H.; Adzic, R. R. J. Phys. Chem. B 2005, 109, 1656316566.

36 Zhang, J.; Vukmirovic, M. B.; Xu, Y.; Mavrikakis, M.; Adzic, R.R. Angew. (2005) Chem., Int. Ed., 44, 2132

37 Stamenkovic, V. R. et al. (2007), Improved oxygen reduction activity on Pt3Ni(111) via increased surface site availability. Science 315, 493–497.

38Stamenkovic, V. R., Mun, B. S., Mayrhofer, K. J. J., Ross, P. N. & Markovic, N. M. (2006) Effect of surface composition on electronic structure, stability and electrocatalytic properties of Pt-transition metal alloys: Pt-skin versus Pt-skeleton surfaces. J. Am. Chem.Soc.128,8813–8819.

39 Stamenkovic, V. R. et al. (2007) Trends in electrocatalysis on extended and nanoscale Ptbimetallic alloy surfaces. Nature Mater. 6, 241–247

40 Paulus, U. A. et al. (2002) Oxygen reduction on high surface areaPt-based alloy catalysts in comparison to well defined smooth bulk alloy electrodes. Electrochim. Acta 47, 3787–3798.

41 Stamenkovic´, V., Schmidt, T. J., Ross, P. N. & Markovic, N. M. (2002) Surface composition effects in electrocatalysis: kinetics of oxygen reduction on well-defined Pt3Ni and Pt3Co alloy surfaces. J. Phys. Chem. B 106, 11970–11979

42 Greeley, J., Stephens, I., Bondarenko, A., Johansson, T., Hansen, H., Jaramillo, T., . . . Norskov, J. (2009). Alloys of platinum and early transition metals as oxygen reduction electrocatalysts. Nature Chemistry,1, 552-556.

43 Gasteiger, H. A., Kocha, S. S., Somappli, B. & Wagner, F. T. (2005). Activity benchmarks and requirements for Pt, Pt-alloy, and non-Pt oxygen reduction catalysts for PEMFCs. Appl. Catal. B-Environ. 56, 9–35

44 Wakisaka, W., Suzuki, H., Mitsui, S., Uchida, H. & Watanabe, M. (2008) Increased oxygen coverage at Pt-Fe alloy cathode for the enhanced oxygen reduction reaction studied by EC-XPS. J. Phys. Chem. C 112, 2750–2755

45 Wagner, F. T. Automotive Challenges and Opportunities for Oxygen Reduction Catalysts. In First CARISMA Intl Conf. (La Grande Motte, France, 23 September 2008).

46 Wang, C. et al. (2010). Monodisperse Pt3Co nanoparticles as electrocatalyst: the effects of particle size and pretreatment on electrocatalytic reduction of oxygen. Phys. Chem. 12, 6933–6939 46.

47 Zhang, J., Yang, H., Fang, J. & Zou, S. (2010) Synthesis and oxygen reduction activity of shape-controlled Pt3Ni nanopolyhedra. Nano Lett. 10, 638–644

48 Zhao, Y., Liu, J., Zhao, Y., & Wang, F. (2014). Composition-controlled synthesis of carbon-supported Pt–Co alloy nanoparticles and the origin of their ORR activity enhancement. Phys. Chem. Chem. Phys.,16(36), 19298-19306. doi:10.1039/c4cp02531h

49 Wang W, Zheng D, Du C, Zou Z, Zhang X, Xia B, Yang H, Akins D L. (2007) Carbon-supported Pd-Co bimetallic nanoparticles as electrocatalysts for the oxygen reduction reaction. Journal of Power Sources,167(2): 243–249

[50] Wu W P, Periasamy A P, Lin G L, Shih Z Y, Chang H T. Palladium copper nanosponges for electrocatalytic reduction of oxygen and glucose detection. Journal of Materials Chemistry A, Materials for Energy and Sustainability, 2015, 3(18): 9675–9681

[51] Peng, X., Omasta, T. J., Roller, J. M., & Mustain, W. E. (2017). Highly active and durable Pd-Cu catalysts for oxygen reduction in alkaline exchange membrane fuel cells. Frontiers in Energy,11(3), 299-309. doi:10.1007/s11708-017-0495-1

[52] Shao M H, Huang T, Liu P, Zhang J, Sasaki K, Vukmirovic M B, Adzic R R. (2006) Palladium monolayer and palladium alloy electrocatalysts for oxygen reduction. Langmuir, 22(25): 1040910415

[53] Ohring, M. (2006). The materials science of thin films. San Diego, Calif: Academic Press.

54 van Dover, R. B. Schneemeyer, L. F. & Fleming, R. M. Discovery of a useful thin-film dielectric using a composition-spread approach. Nature 392, 162–164 (1998).

55 Briceno, G., Chang, H., Sun, X., Schultz, P. G. & Xiang, X.-D. A class of cobalt oxide magnetoresistance materials discovered with combinatorial synthesis. Science 270, 273–275 (1995).

56 Xiang, X.-D. et al. (1995).A combinatorial approach to materials discovery. Science 2268, 1738–1740.

57 Danielson, E. et al. (1997). A combinatorial approach to the discovery and optimization of luminescent materials. Nature 389, 944–948.

58 I. Langmuir, (1929), Phys. Rev. 33, 954.

[59] B. Dong, L. Taylor, P-Y. Hsu., Brief introduction of Using Fenris. Also from: http : //www.umms.sav.sk/6493 en/physical − vapor − deposition/

[60] G. C. Stutzin, K. Rozsa, and A. Gallagher, J. (1993), Vac. Sci. Technol. A11, 647.

[61] Mitterer, C., Heuzb, O., & Derttinger, V. (1997). ELSEVIER Z / glltVOlO l Substrate and coating damage by arcing during sputtering. Surface and Coatings Technology, 89, 233–238.

[62] Anders, A. (2006). Physics of arcing, and implications to sputter deposition. Thin Solid Films, 502(1–2), 22–28. https://doi.org/10.1016/j.tsf.2005.07.228

[63] D. L. Smith, (1995), Thin-Film Deposition. McGraw-Hill, New York,

[64] Notice of Proposed Rule Making. (2016). *Journal of the American Pharmaceutical Association (1961)*, *15*(3), 145–150. https://doi.org/10.1016/s0003-0465(15)31998-4

[65] Maissel, L. I., & Schaible, P. M. (1965). Thin films deposited by bias sputtering. *Journal of Applied Physics*, *36*(1), 237–242. https://doi.org/10.1063/1.1713883

[66] Erik Reddington, Anthony Sapienza, Bogdan Gurau, Rameshkrishnan Viswanathan, S. Sarangapani, Eugene S. Smotkin, Thomas E. Mallouk, (1998). Combinatorial Electrochemistry: A Highly Parallel, Optical Screening Method for Discovery of Better Electrocatalysts. Science, 1998, 280, 1735,

[67] S. Jayaraman and A. C. Hillier. (2003). Screening the Reactivity of Pt_xRu_y and $Pt_xRu_yMo_z$ Catalysts toward the Hydrogen Oxidation Reaction with the Scanning Electrochemical Microscope. J. Phys. Chem. B, 107, 5221-5230.

[68] S. Jayaraman and A. C. Hillier, (2004). Construction and Reactivity Screening of a Surface Composition Gradient for Combinatorial Discovery of Electro-Oxidation Catalysts. J. Comb. Chem. 6, 27-31.

[69] Jose L. Fernandez, Darren A. Walsh, and Allen J. Bard, (2005). Thermodynamic Guidelines for the Design of Bimetallic Catalysts for Oxygen Electroreduction and Rapid Screening by Scanning Electrochemical Microscopy. M-Co (M: Pd, Ag, Au). *J. Am. Chem. Soc*. 127, 357-365

[70] M. E. Tague, J. M. Gregoire, A. Legard, E. Smith, D. Dale, R. Hennig, F. J. DiSalvo, R. B. van Dover, Abruña, H. D. (2012) High Throughput Thin Film Pt-M Alloys for Fuel Electrooxidation: Low Concentrations of M (M = Sn, Ta, W, Mo, Ru, Fe, In, Pd, Hf, Zn, Zr, Nb, Sc, Ni, Ti, V, Cr, Rh) *J. Electrochem. Soc.* 159, F880-F887.

[71] J. M. Gregoire, M. E. Tague, S. Cahen, S. Khan, Abruña, H. D., Francis J. DiSalvo, R. Bruce van Dover, (2010). Improved Fuel Cell Oxidation Catalysis in $Pt_{1-x}Ta_x$. Chem. Mater. 22, 1080-1087

[72] Prochaska, M.; Jin, J.; Rochefort, D.; Zhuang, L.; DiSalvo, F. J.; Abruña, H. D.; van Dover, R. B. (2006). High throughput screening of electrocatalysts for fuel cell applications. REVIEW OF SCIENTIFIC INSTRUMENTS, 77, 054104.

[73] Sanmita Inc. (2017, May 19). Tencor AlphaStep 500. Retrieved from http://www.ccmr.cornell.edu/instruments/tencor-alpha-step-500/

[74] Sanmita Inc. (2018, November 13). Bruker D8 General Area Detector Diffraction System (GADDS). Retrieved from https://www.ccmr.cornell.edu/instruments/bruker-general-area-detector-diffraction-system-gadds/

[75] Sanmita Inc. (2017, November 06). SEM skipping generations ahead (Nov 2017). Retrieved from https://www.ccmr.cornell.edu/news/sem-skipping-generations-ahead/

[76] Fuller, T. F., Harb, J. N., & Harb, J. N. (2018). *Electrochemical Engineering*. Somerset: John Wiley & Sons, Incorporated.

[77] Bard, A. J., & Faulkner, L. R. (2001). *Electrochemical methods: Fundamentals and applications*. New York: Wiley.

[78] Cliff, G.; Lorimer, G. W. (1975) The Quantitative Analysis of Thin Specimens. J. Microsc., 103, 203-207.

79 Denton, A. R., & Ashcroft, N. W. (1991). Vegard Law. Physical Review A, 43(6), 3161–3164.

[80] Ghosh, G., Kantner, C., & Olson, G. B. (1999). Thermodynamic modeling of the Pd-X (X=Ag, Co, Fe, Ni) systems. *Journal of Phase Equilibria,20*(3), 295-308. doi:10.1361/105497199770335811

[81] Li, M., Du, Z., Guo, C., & Li, C. (2008). A thermodynamic modeling of the Cu–Pd system. *Calphad,32*(2), 439-446. doi:10.1016/j.calphad.2008.04.004

82 Goldbeck, O. K. (1982). Fe—Pd Iron—Palladium. *IRON—Binary Phase Diagrams,*88-91. doi:10.1007/978-3-662-08024-5_49

83 Davis, R. E.; Horvath, G. L.; Tobias, C. W. (1967), The Solubility and Diffusion Coefficient of Oxygen in Potassium Hydroxide Solutions. Electrochim. Acta, 12, 287-297

84 Yang, Y.; Wang, Y.; Xiong, Y.; Huang, X.; Shen, L.; Huang, R.; Wang, H.; Pastore, J. P.; Yu, S. H.; Xiao, L.; Brock, J. D.; Zhuang, L.; Abruña, H. D. (2019) In Situ X-Ray Absorption Spectroscopy of a Synergistic Co-Mn Oxide Catalyst for the Oxygen Reduction Reaction. *J. Am. Chem. Soc. 141*, 1463–1466.

85 Okamoto, H. (1993). Mn-Pd (manganese-palladium). *Journal of Phase Equilibria,14*(5), 654-655. doi:10.1007/bf02669165

86 Ghosh G., and Olson G.B. (2000). Thermodynamic Modeling of the Cr-Pd and Mo-Pd Systems. Journal of Phase Equilibria Vol. 21, p 32-39

87 Massalski, T. B. (1980). The binary phase diagram evaluation program. *Bulletin of Alloy Phase Diagrams,1*(2), 32-34. doi:10.1007/bf02881175

88 Okamoto H., (1993). Pd-Ti (Palladium-Titanium), J. Phase Equilib., Vol. 14, p 128-129

89 Denton, A. R., & Ashcroft, N. W. (1991). Vegard Law. *Physical Review A*, *43*(6), 3161–3164.

90 Dai, H. (2012). *Covalent Hybrid of Spinel Manganese − Cobalt Oxide and Graphene as Advanced Oxygen Reduction Electrocatalysts*. *c*. https://doi.org/10.1021/ja210924t

91 Lomholt, H. (1992). *Surface energy and work function of elemental metals Publication date :* https://doi.org/10.1103/PhysRevB.46.7157

92 Palladium Price: Palladium Price Chart History: Price of Palladium Today. (n.d.). Retrieved from https://www.apmex.com/spotprices/palladium-price

[93] Gleason, S. (2019, June 17). Platinum Spot Price Live & Historical Chart: Quotes in USD. Retrieved from https://www.moneymetals.com/precious-metals-charts/platinum-price

[94] Palladium Prices - Interactive Historical Chart. (n.d.). Retrieved from https://www.macrotrends.net/2542/palladium-prices-historical-chart-data

[95] Lomholt, H. (1992). *Surface energy and work function of elemental metals Publication date :* https://doi.org/10.1103/PhysRevB.46.7157

[96] Buchanan, C., & Gardner, L. (2019). Metal 3D printing in construction : A review of methods , research , applications , opportunities and challenges. *Engineering Structures*, *180*(March 2018), 332–348. https://doi.org/10.1016/j.engstruct.2018.11.045

[97] Buchanan, C., & Gardner, L. (2019). Metal 3D printing in construction : A review of methods , research , applications , opportunities and challenges. *Engineering Structures*, *180*(March 2018), 332–348. https://doi.org/10.1016/j.engstruct.2018.11.045